

FEATURE ARTICLE

View Article Online



Cite this: Chem. Commun., 2023, **59**, 4852

Design principles for the synthesis of platinum-cobalt intermetallic nanoparticles for electrocatalytic applications

Siying Yu and Hong Yang *

As the development of polymer electrolyte membrane fuel cells (PEMFCs) has sped up in recent years, producing active and durable electrocatalysts has become an increasingly important technical challenge. Platinum-cobalt (Pt-Co) alloy electrocatalyst has been commercially applied to hydrogen-powered fuel cell vehicles, and their intermetallic forms promise better durability, which is crucial to satisfy the 8000 h lifetime target of heavy-duty vehicles and other transportation options. In this feature article, we first present the atomically ordered structures of Pt-Co intermetallic, then discuss the thermodynamic and kinetic driving forces for making the PtCo-based intermetallic nanoparticles with desired structural attributes, followed by recent examples to illustrate how to achieve better control in composition, size, and shape. Discussion on the relationship between the key structural features and catalytic performance is focused on the application of Pt-Co intermetallic nanostructures as oxygen reduction reaction (ORR) electrocatalysts for hydrogen-powered PEMFCs. We emphasize specifically the importance of intermetallic structures for enhancing the durability and summarize the characterizations of their electrocatalytic performance in both three-electrode system and full cell studies. Finally, we provide our perspectives on the design, synthesis, characterization, and property studies of Pt-Co intermetallic nanoparticles as ORR electrocatalysts. This article should provide a new understanding on the design of ORR electrocatalytic applications using this class of intermetallics.

Received 9th February 2023, Accepted 20th March 2023

DOI: 10.1039/d3cc00590a

rsc.li/chemcomm

Department of Chemical and Biomolecular Engineering, University of Illinois at Urbana-Champaign, 206, Roger Adams Laboratory, 600 South Mathews, Urbana, IL, 61801, USA, E-mail: hv66@illinois.edu



Siying Yu

Siying Yu received her BSc degree Chemistry from Peking University in 2019. She then joined Professor Hong Yang's group at the University of Illinois at Urbana-Champaign (UIUC) as a PhD student in the same year. Her graduate research has focused on the development and characterization of low-PGM electrocatalysts for fuel cell applications, non-precious metal catalysts for water electrolysis and thermal catalysis.



Hong Yang

Hong Yang is the Richard C. Alkire Chair Professor Chemical Engineering at UIUC. He received his PhD degree in 1998 from University of Toronto and did his postdoctoral training as an NSERC Postdoctoral Fellow at Harvard University. He worked University of Rochester between 2001 and 2011 and moved to UIUC in 2012. He is an elected Fellow of AAAS, a winner of the Doctoral Prize from NSERC Canada, and a

recipient of the CAREER Award from US NSF. His current research interests are in material chemistry approach to the development of nanostructures for catalysis, energy, and sustainability applications.

1. Introduction

Precious metals such as gold (Au), silver (Ag), and platinum (Pt) have been recognized as valuable elements since ancient times. In modern days, their excellent stability, unique surface-related physiochemical properties, and biocompatibility ensure that they continue to play critical roles in a range of important industrial applications, such as petroleum cracking,1 exhaust treatment,2 nanomedicine,3 and lately electrocatalysis for sustainability. 4-8 Among precious metals, Pt-based materials have exhibited superior activitiy^{4,9,10} and better durability^{11,12} when catalyzing the oxygen reduction reaction (ORR), which is the cathodic half-reaction in polymer electrolyte membrane fuel cells (PEMFCs) for hydrogen-powered transportation applications.

As the need for large PEMFCs surges, targeting heavy-duty applications, 13 it becomes an acute issue to utilize Pt most effectively. The incorporation of early transition metals (i.e., Fe, 14,15 Co, 16,17 and Ni, 18,19) and the nano-engineering of Pt-based electrocatalysts are the key technological solutions. 16,19-23 Platinum-based bimetallic nanoparticles (NPs) often exhibit higher ORR activity than pure Pt electrocatalysts, partly because of the strain and ligand effects.^{24,25} Alloying with a 3d transition metal shifts the d-band of Pt downward, 26 decreases the adsorption energy of oxygen species on the surfaces, 27 lowers the activation energy barrier, and, as a consequence, enhances the ORR performance.

Nanostructures of Pt-based bimetallic NPs directly affect their electrocatalytic properties. Upon the completion of initial activation, these electrocatalysts often have an alloy (or intermetallic) core and Pt-rich shell, or skin layer, which is regularly observed under a scanning transmission electron microscope (STEM). 28,29 The formation of Pt shell is due to the leaching of non-noble metals under acidic operating conditions,30 and through the diffusion of Pt atoms with or without thermal treatment. 31,32 The Pt skin not only serves as a protective layer against further dissolution but also induces surface strain from the lattice mismatch with the alloy (or intermetallic) cores underneath. 30,33,34 Besides the composition and surface structures, nanoengineering is often used to control the particle size, which impacts more than the improvement of the atomic utilization of precious metals. There is a tradeoff between increasing specific surface area to expose more active sites and decreasing surface energy to improve the structural stability. The optimal size for Pt-based bimetallic NPs was found to be about 5 nm, which exhibits peak catalytic activity³⁵ and may possess an oxophilic surface layer (PtOx) to inhibit further metal dissolution during the cell operations.³⁶

While recent research has drastically improved the ORR activity of Pt-based electrocatalysts through the control of composition, size, and shape, a major challenge for their applications, especially in heavy-duty areas, rises from the chemical and structural instability of Pt-based alloy NPs under harsh PEMFC operational conditions. A variety of Pt-based alloy electrocatalysts exhibit an ORR mass activity of > 0.44 A mg_{Pt}⁻¹ the benchmark value set by the department of energy (DOE)³⁷

using the rotating disk electrode (RDE) technique after the standard accelerated stress tests (ASTs, typically for 30 k cycles).38 However, only a small portion of these electrocatalysts can retain high performance (>0.44 A mg_{Pt}⁻¹) in membrane electrode assembly (MEA). 16,39 Among them, the Pt-Co alloy electrocatalyst has been used in hydrogen-powered fuel cell vehicles. 40 Thus, the Pt-Co-based intermetallic, which exhibits long-range atomic order, is considered as a promising electrocatalyst to meet the DOE performance target of 8000 h system durability for PEMFCs used in heavy duty vehicles.

In this feature article, we start with the analysis of structures of Pt-Co intermetallics, followed by discussions of thermodynamic and kinetic factors in controlling the production of intermetallic NPs. Recent examples on how to control composition, size, and shape and their applications in electrocatalysis will then be presented. It should be noted that there are reviews on Pt-based alloy and intermetallic nanoparticles published previously, 8,20,41-52 and this feature article is focused on Pt-Co intermetallic NPs. Papers on Pt-Co alloys are largely not included in this feature article.^{7,53} Strictly speaking, an intermetallic compound is highly exothermic in the formation from constituent metals and possesses different physical and mechanical properties (e.g., brittleness, hardness, and high melting point) than its alloy counterpart in the bulk; we, however, focus on the atomic structure of the nanoparticles. Thus, we adopt the convention of using X-ray diffraction (XRD) as the method to characterize if a Pt-Co bimetallic nanostructure exists as an intermetallic or not.

2. Structures of platinum-cobalt intermetallic nanoparticles

The primary difference between an alloy and an intermetallic is atomic ordering. Alloy is a disordered solid solution consisting of two or more metal elements with flexible, non-stoichiometric ratios. The structures of alloys may be determined by the symmetry of constituent metals that randomly occupy the lattice points of a crystal. For example, Pt-Co alloys have facecentered cubic (fcc) structure, the same as that of the fcc phase of Pt or Co metal. On the other hand, an intermetallic is composed of an ordered array of metal atoms sitting on the lattice points, forming a compound of the constituent metals with long-range ordering. The stoichiometry of the intermetallic is well-defined. In this context, each intermetallic phase can be regarded as a new compound with a defined unit cell that may be identified by a distinctive XRD pattern.

Fig. 1a illustrates the unit cell structures and low-index facets of three Pt-Co intermetallic structures: L12-Pt3Co, L10-PtCo, and L12-PtCo3. L10-PtCo has a tetragonal crystalline phase, in which layers of Pt and Co atoms stack alternatively along the c axis. The L1₂ structure exists in a cubic phase, with one type of metal atoms occupying all six face centers and the other one occupying all eight corners. These intermetallic compounds exhibit very different XRD patterns when compared with Pt; thus, XRD is the most efficient and straightforward

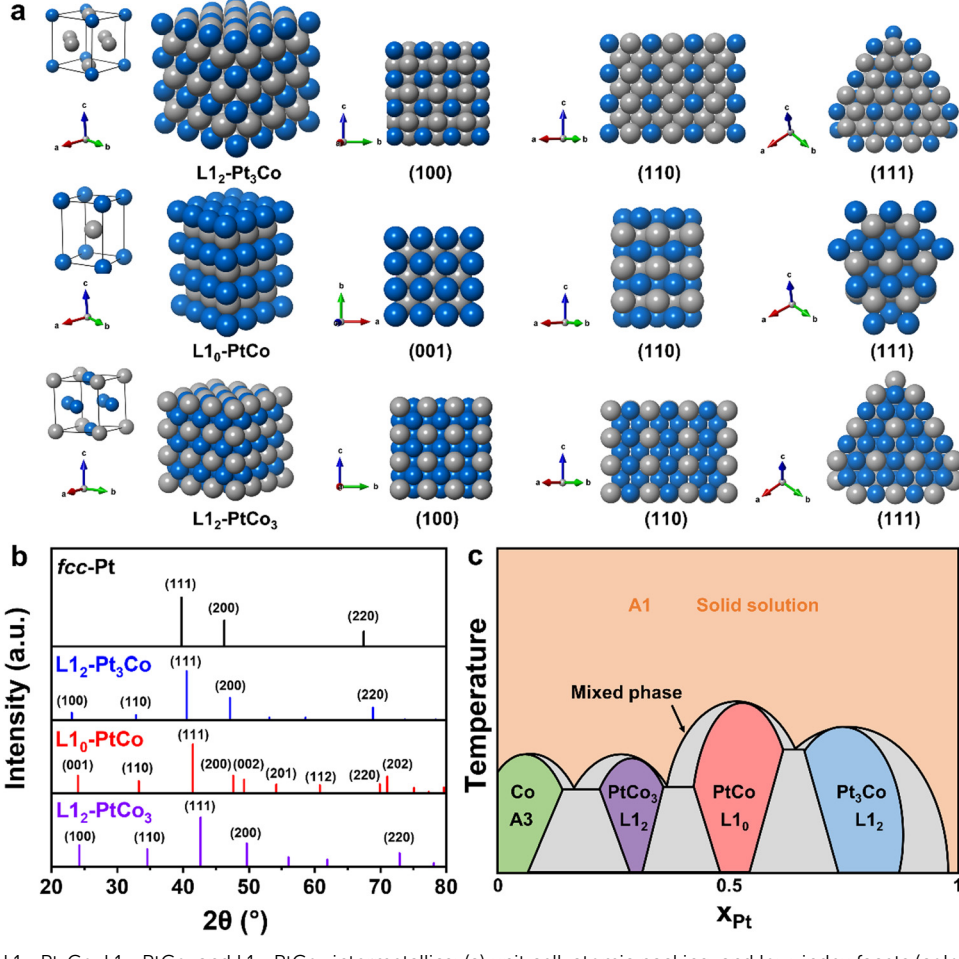


Fig. 1 Illustrations of L1₂-Pt₃Co, L1₀-PtCo, and L1₂-PtCo₃ intermetallics: (a) unit cell, atomic packing, and low-index facets (color code: blue-Co, grey-Pt), (b) XRD patterns for fcc-Pt (PDF#04-0802), $L1_2$ -Pt₃Co (PDF#29-0499), $L1_0$ -PtCo (PDF#43-1358), and $L1_2$ -PtCo₃ (obtained from VESTA simulation, using unit cell parameters from reported $PtCo_3$ alloy structure⁵⁸), and (c) conceptualized Pt-Co phase diagram.

method to characterize the Pt-Co intermetallics (Fig. 1b). In this article. XRD characterization is used as the indicator for the formation of intermetallics and the determination of their specific structures (L1₀ or L1₂).

Fig. 1c illustrates the typical Pt-Co phase diagram drawn based on theoretical calculation.⁵⁴ The most commonly observed Pt-Co intermetallic phases are L10-PtCo and L12-Pt₃Co. While L1₂-PtCo₃ has been predicted by simulation,⁵⁴ there is sparse experimental evidence.^{55–57} In this perspective, we will cover primarily the L10-PtCo intermetallic and, to a lesser degree, the L1₂-Pt₃Co phase because of their applications in electrocatalysis.

3. Design principles for the synthesis of Pt-Co intermetallic nanoparticles

3.1. Thermodynamic and kinetic driving forces

Platinum-cobalt intermetallic nanoparticles are typically made from their alloy counterparts through thermal treatment. 30,59 The thermodynamics for making intermetallics from alloys via such a treatment can be understood based on the change in the Gibbs free energy of the ordering process (ΔG_0) at a given temperature (T), which can be written as

$$\Delta G_{0} = \Delta H_{a \to i} - T \Delta S_{a \to i} \tag{1}$$

where $\Delta H_{a \to i}$ is the change in the enthalpy and $\Delta S_{a \to i}$ is the change in the entropy from the disordered alloy (a) to the ordered intermetallic (i) phases. For the alloy and intermetallic, with the same constituent metals and stoichiometry, $\Delta H_{a \rightarrow i}$ is negative due to the stronger Pt-M bonds in an ordered array (intermetallic) than that in a random array (alloy). 43,44 $\Delta S_{a\rightarrow i}$ is negative as well because entropy is interpreted as the degree of disorder or randomness in the system. Thus, the less disordered structure has a smaller value of S. Since temperature (T) has the unit of K, the second term $(-T\Delta S_{a\rightarrow i})$ is positive and its value increases monotonically with elevated temperature. The relationship between ΔG_0 and T can be conceptually depicted (Fig. 2). The ordering process is thermodynamically favored when the value of T satisfies the condition $\Delta G_0 < 0$. In another word, when temperature is high enough, the thermodynamically stable structure is an alloy, which explains the "A1 solid solution" area in the Pt-Co phase diagram (Fig. 1c).

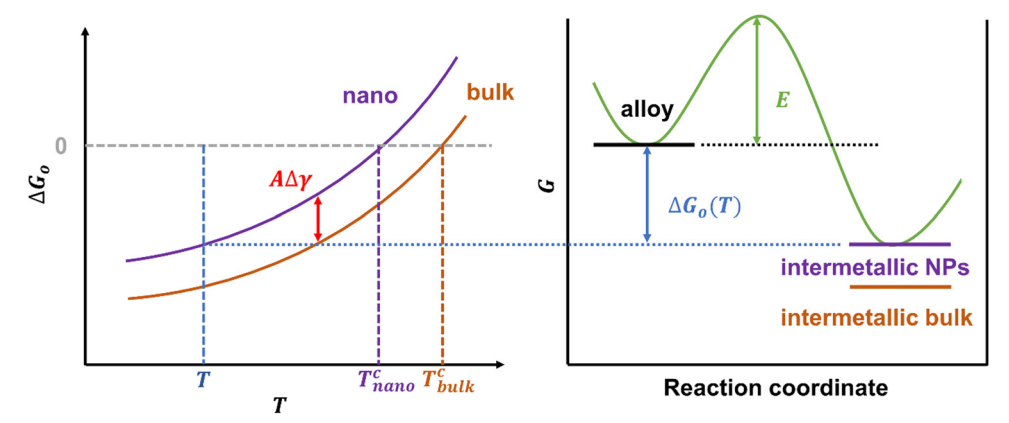


Fig. 2 Illustration of change in Gibbs free energy of the process of atomic ordering (ΔG_0) from alloy to intermetallic phases and the corresponding reaction coordinates

The value of T at the critical point where ΔG_0 is zero is defined as the critical phase-transition temperature (T^c) , below which the intermetallic structure is energetically favored (Fig. 2, the coordinate on the left). When the size is reduced to the nanometer scale, the surface energy must be taken into consideration because of the dramatic increase in the number of surface dangling bonds and specific surface area. Thus, the extra surface energy term $(A\Delta \gamma_{a\rightarrow i})$ needs to be added to calculate ΔG_0 value for this process.

$$\Delta G_{0} = \Delta H_{a \to i} - T \Delta S_{a \to i} + A \Delta \gamma_{a \to i} \tag{2}$$

where A is the surface area and $\Delta \gamma_{a \to i}$ is the change of surface energy. The intermetallic has a higher surface energy than the alloy due to the higher bond energy, resulting in a higher value of ΔG_0 for a given temperature, which narrows the feasible temperature range of the ordering process. As is shown in Fig. 2, the critical phase-transition temperature of nanomaterial $(T_{\text{nano}}^{\text{c}})$ is smaller than that of the bulk material $(T_{\text{buk}}^{\text{c}})$. More importantly, for a given T, the increased $\Delta G_0(T)$ implies a smaller energy drop (equal to the absolute value of ΔG_0), which makes the intermetallic structure less thermodynamically favorable at the same temperature (Fig. 2, the coordinate on the right). Meanwhile, the synthesis of Pt-based intermetallic NPs often requires an additional annealing step to overcome the activation energy barrier (E) from the disordered to the ordered structure.

The dependence of the reaction rate on temperature can be described by the logarithmic analysis. A simplified kinetic model of disorder-to-order transition can be treated as a combination of new phase formation within the parent phase (nucleation) and material transport (diffusion).44 Thus, the overall rate for the formation of intermetallic from alloy can be written as the product of new phase formation rate f(T) and diffusion rate D(T).

$$R(T) = f(T)D(T) \tag{3}$$

The new phase formation rate f(T) is closely related to the formation energy of the intermetallic, while the diffusion rate D(T) depends on atom-exchange mechanisms. Under the assumption that the diffusion of metal atoms can be regarded as a simple lattice jump from their original positions to neighboring vacancies, an intermetallic structure with relatively weak Pt-M bond tends to have both low defect formation energy and low jumping barrier. 44 Atom diffusion may significantly accelerate when the reaction temperature rises. This model may be sufficient to understand the general formation; understanding the local ordering mechanism at the atomic scale, however, still requires advanced experimental technigues, such as high resolution in situ microscopy, which enables the characterization of the Pt-Co ordering process (see the examples discussed in Section 3.2).

3.2. Atomic ordering

At the atomic scale, the formation of the intermetallic phase corresponds to the ordering of atoms at a long coherent length. An intermetallic structure is thermodynamically stable below the critical temperature (T^c) but requires activation energy to complete the disorder-to-order transition. It is rare to obtain a perfectly ordered intermetallic structure since most Pt-Co intermetallic NPs inevitably contain disordered regions. Thus, the degree of ordering (S^2) is used to quantitatively describe the transition from the alloy to the intermetallic phase. Experimentally, the degree of ordering (S^2) may be estimated based on the XRD data using the following equation.^{60,61}

$$S^{2} = \frac{\{I_{110}/I_{111}\}_{\text{measured}}}{\{I_{110}/I_{111}\}_{\text{f}}} \tag{4}$$

where $\{I_{110}/I_{111}\}_{\rm measured}$ and $\{I_{110}/I_{111}\}_{\rm f}$ are the integrated intensity ratios between (110) and (111) diffractions obtained from the measurement of a sample and the simulation of the fullyordered intermetallic (L10 or L12 for Pt-Co) phase, respectively. The degree of ordering is an important structural factor when evaluating the structural properties as it affects the activity 60,62 and durability⁶¹ of Pt-Co intermetallic NPs as electrocatalysts.

The ordering process is often studied using high-resolution microscopic characterization techniques. High-resolution transmission electron microscopy (TEM) study can be used to examine the dynamics of a range of Pt bimetallic nanostructures and

to the center of nanoparticles.

provide critical clues and details for developing the proper processes. 31,32,61,63-69 Recent in situ TEM study reveals the continuous but distinctive stages of surface rearrangements to form the intermetallic phase during the annealing of Pt₃Co nanoparticles: (1) initial alloy elemental distribution, (2) formation of surface Pt-skin layer, (3) nucleation of structurally ordered domains, and (4) development of ordered framework.³² Segregation of Pt onto the surface was highly sensitive to the annealing temperature. It was driven by a negative enthalpy for surface segregation when below 550 °C. With the annealing temperature increased, the disorder-to-order transformation was initiated on the Pt₃Co {110} facets, which had the largest driving force according to density functional theory (DFT) calculations. The newly formed ordered structure then continued to propagate on the {001} planes inward

Besides the mode of formation through continuous evolution, phase transition to intermetallic may compete with surface diffusion in the ordering process, as observed in the synthesis of L12-Pt3Co NPs.63 The two formation modes are surface diffusion-induced phase transition (SDIPT) and reconstruction-induced body phase transition (RIBPT). SDIPT occurred mainly on the surface layer, involving a long-range diffusion driven by the surface chemical potential gradient, while RIBPT referred to atomic reconstruction inside the crystal within a short range. These two competing modes could work synergistically to produce the L1₂-Pt₃Co structure with different morphologies. When Pt₃Co alloy nanoparticles went through low-temperature diffusion annealing process (LTDAP) and reached 600 °C, the process occurring on the {100} facet could be categorized into three stages, according to the growth rate of intermetallic in the two formation modes: (1) SDIPT-dominated stage, (2) SDIPT and RIBPT competitive stage, and (3) RIBPTdominated stage. Depletion of low-coordination (CN) surface atoms decelerated SDIPT in the later stages, and RIBPT gradually took over after the energy for short-range reconstruction became larger than the barrier of nucleation in the second stage (Fig. 3a). For the {110} facet, however, corner atoms preferred to move away from the site instead of undergoing phase reconstruction in the first stage. This process was called "low-coordination (CN) atom losing stage." The loss of atoms at the corners left behind large amounts of defects and vacancies, leading to the defect-driven rapid growth at the second stage. Consequently, phase reconstruction also became easier than before because of the rich defects and vacancies in the second stage. The third stage is RIBPT-dominated slow growth as the intermetallic region propagated inward with diminishing vacancies and defects. If the Pt₃Co alloy nanoparticles were treated via the direct high-temperature annealing process (DHTAP) at 700 °C, the ordered phase started to form at the outermost later of the {100} facet (Fig. 3b), but intermetallic growth on the {110} facets slowed down. In general, SDIPT under DHTAP conditions was slower than RIBPT, and the corner atoms did not have sufficient time to diffuse onto the {100} facets. This sluggish diffusion under DHTAP resulted in more corner atoms than LTDAP; thus, cubic and spherical products were generated, respectively (Fig. 3c).

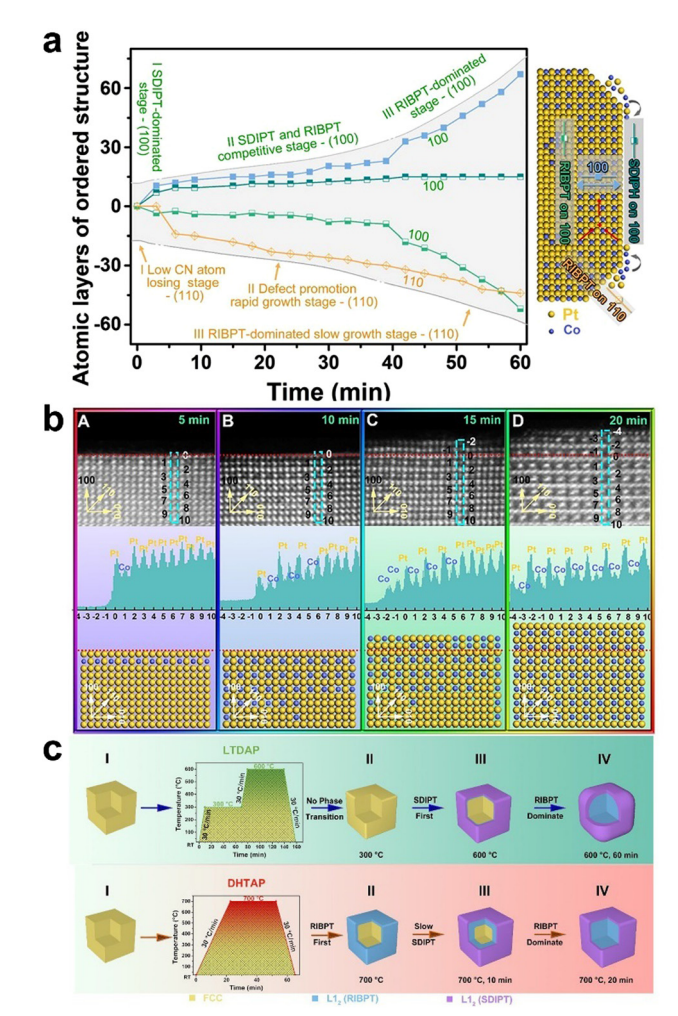


Fig. 3 Reconstruction and surface diffusion-induced phase transition behavior along the [100] and [110] directions of the Pt₃Co intermetallic. (a) Changes in the atomic layers of the ordered L1₂-Pt₃Co intermetallic nanocrystals as a function of time along the two directions. (b) Layer-bylayer growth of the ordered Pt₃Co during annealing. Enlarged high-angle annular dark field (HAADF)-STEM images of the {100} surface, the intensity profiles taken from the surface marked by rectangles, and the corresponding atomic model of enlarged HAADF-STEM images acquired at 700 °C for (A) 5 min, (B) 10 min, (C) 15 min, and (D) 20 min. (c) Schematic representation of the dynamic process of the Pt₃Co cubes under LTDAP and DHTAP, respectively. Reproduced with permission from ref. 63. Copyright 2021, American Chemical Society.

Besides atomic ordering from the Pt-Co alloy NPs, the formation of an intermetallic structure can also be the result of diffusion of Co atoms into Pt NPs. 64 CoN4-rich carbon (Co/ NC) was shown to be a viable precursor and could be prepared from zeolitic imidazolate framework-8 (ZIF-8). This precursor was used as both the support and the Co source (Fig. 4a). At a mass loading of 20 wt%, Pt NPs formed on the CoN4-rich carbon and was subsequently alloyed with Co atoms. STEMenergy-dispersive X-ray (EDX) mapping study indicates that as the temperature increased from room temperature to 1000 °C, Co atoms gradually diffused into the lattice of Pt NPs (Fig. 4b). The atomic ratio between Co and Pt eventually increased to ~ 0.3 (Fig. 4c). This observation confirmed that Pt-Co

900℃ N₂3h Pt NP Deposition Thermal Treatment Pt Atomization Co/ZIF8@F127 Co/NC 6PtSA-Co C 200 ℃ 1000 °C 800 intermetallic 0.20 ColPt 010

Fig. 4 (a) Schematic illustration showing the synthesis of PtCo/NC (nPtCo/NC, n represents the mass loading of Pt, n = 20 or 6 wt%). Observation of the dynamic process of alloying between Pt and Co during the thermal treatment; (b) EDX mapping of Pt (red) and Co (green) species in the 20PtCo/NC

sample after annealing at 200, 600, 800, and 1000 °C, respectively (scale bar: 10 nm). (c) Atomic ratio between Co and Pt as functions of temperature and

intermetallic NPs could be made through the diffusion of Co atoms into Pt NPs as well. In situ environmental TEM was used to examine the atomic ordering, including the study of mechanisms of metal segregation and particle coalescence. 31,32,65,70

time. Reproduced with permission from ref. 64. Copyright 2021, Wiley-VCH.

3.3. Composition control

Feature Article

In principle, it is easier to control the composition of intermetallics than alloys in the formation of Pt-based bimetallic NPs⁷¹ because the stoichiometry of intermetallics is well defined.⁷² In practice, a stoichiometric ratio obtained from the phase diagram might still be locally inhomogeneous.44 Metal segregation,⁷³ especially the surface segregation of Pt, is a commonly observed phenomenon. Surface segregation often occurs after heat^{28,29,31,65} or acid treatment³⁰ of the Pt-based bimetallic. The formation of the Pt-rich shell changes the overall stoichiometric ratio for the intermetallic NPs. The existence of the Pt shell, however, can be beneficial, because this surface structure may improve both the activity and durability of electrocatalysts. 30,33,34 Controlling the feeding ratio is thus needed to achieve the required stoichiometry with Pt-enriched skin layer or shell.44,74

For Pt-Co, the two most commonly observed intermetallic phases are L1₀-PtCo and L1₂-Pt₃Co. Theoretical simulation suggests that these two intermetallic structures are energetically favored in the similar temperature range (Fig. 1c).⁵⁴ As a result, the procedures for making either intermetallic can be similar, except for the amount of metal precursors added to the synthetic mixture. 33,75 L12-PtCo3 has been theoretically proposed but with few experimental observations. 56,57 Small L12-PtCo3 intermetallic NPs on carbon were obtained by spray dehydration, followed by annealing.⁵⁵ The XRD pattern was used to determine the formation of this intermetallic phase by comparing it with the standard diffraction pattern from L12-PtFe₃ (PDF#71-8365). A slight positive shift in the 2θ angle was observed because Co has a smaller atomic radius than Fe. The L12-PtCo3 intermetallic NPs are hard to produce, presumably because Co prefers to exist in the hcp phase at ambient temperature, which has a large lattice mismatch with fcc Pt. It should be noted that the stoichiometric ratio of the final product is helpful to verify the intermetallic structure, but it does not necessarily imply whether the intermetallic is L10-PtCo, L12-Pt3C, or L12-PtCo3. Both metal segregation and local inhomogeneity can lead to an intermetallic structure with very different Pt/Co ratio.76 It is a common practice to use XRD to characterize and confirm the crystal structures of the Pt-Co intermetallics and rely on high resolution STEM for detailed atomic information. It is noteworthy that an intermetallic does not follow the relationship between the lattice parameters and atomic content, as defined by Vegard's law for a solid solution (i.e., random alloy). Even if the composition is nonstoichiometric, Pt-Co NPs can still show intermetallic features in characterization, such as XRD.

A third metal can be added to a Pt-Co intermetallic to modify its surface and core structures, and thus its catalytic properties. The incorporation of additional metal(s) into the crystal lattice raises the question whether such NPs can still be called "intermetallic", since, strictly speaking, at least one lattice site no longer has long-range ordering or specific stoichiometry in the bimetallic structures, as shown in Fig. 1a. In this feature article, we coin the term "half-intermetallic" to

ChemComm Feature Article

describe a ternary or multimetallic system, in which one lattice site (i.e., Pt) is fully ordered, while the other lattices site is occupied by secondary metal atoms (i.e., non-Pt metals) that can be randomly distributed. 77-79 The amount of the incorporated metal is typically small (<10 at%). For example, tungsten (W) atom was reported to be incorporated into L1₀-PtCo NPs to form a half-intermetallic of W_{0.05}PtCo.⁸⁰ Theoretical calculations and extended X-ray absorption fine structure (EXAFS) analysis revealed that W atoms stabilized the intermetallic structure, tuned the Pt-Pt distance, and changed its binding energy with oxygen species. The incorporation of Cu into the L1₀-PtCo intermetallic was also reported to form a halfintermetallic $PtCo_xCu_{1-x}$ (x = 0.25, 0.5, 0.75). 81 A rationale for making a half-intermetallic is to tune the Pt-Pt distance to improve its catalytic activity.

3.4. Size control

Size plays important roles in determining the properties of Ptbased intermetallic NPs. 82 Small NPs have high specific surface area that often results in exposing a large population of active sites. However, when the size is too small (diameter $< \sim 2$ nm. assuming a spherical shape), the performance may suffer as well. Finding the optimal size can balance the catalytic activity and durability.35,36 For Pt-Co intermetallic NPs, there also exists a size-dependent structural ordering.83-85

While controlling the size of the bimetallic alloy may be straightforward, it can be challenging for intermetallic NPs since high-temperature annealing (>500 °C) is generally required to overcome the energy barrier for atomic ordering.⁸⁶ Based on the Gibbs-Thomson equation, the chemical potential of the surface region of a nanoparticle (μ) can be written as follows.

$$\mu = k_{\rm B} T \ln \left[c_{\rm eq}(r) \right] = \frac{2\sigma v_{\rm at}}{r} \ln \left[c_{\rm eq}(\infty) \right] \tag{5}$$

$$c_{\rm eq}(r) = c_{\rm eq}(\infty) \exp\left(\frac{2\sigma v_{\rm at}}{rk_{\rm B}T}\right)$$
 (6)

where $c_{\rm eq}(\infty)$ is the solubility of atoms taken from an infinite flat surface, σ is the surface tension, v_{at} is the atomic volume, r is the surface curvature, and $k_{\rm B}$ is the Boltzmann constant. The reciprocal relationship between chemical potential μ and surface curvature r implies that atoms tend to diffuse to surfaces with a large curvature radius. Ostwald ripening and particle coalescence⁸⁷ may occur simultaneously during the process, resulting in the formation of polydisperse and larger intermetallic NPs. The key to size control, based on the discussion above, is to inhibit the atomic diffusion and particle migration during the heat treatment process. For Pt-Co intermetallic NPs, enhancing the support-metal interaction and applying spatial confinement are two main approaches to size control. Both methods promote the uniform dispersion of metal precursors.

3.4.1. Support-metal interaction. The electrostatic adsorption of ions on protonated or charged surfaces can enhance supportmetal interaction.^{59,88} Fine L1₀-PtCo intermetallic NPs were made by anchoring metal complexes on N-doped carbon using the strong electrostatic adsorption (SEA) technique.⁵⁹ This anchoring effect

provides locally stabilized metal species, preventing atoms from migration and aggregation during the mixing and heating process. The surface of the support could be either positively or negatively charged by adjusting the pH values in either side of the point of zero charge (PZC) (Fig. 5a). The metal precursors have opposite charges electrostatically adsorbed onto the surface. One advantage of electrostatic adsorption is that the support-metal interaction is tunable by adjusting the pH value. Fig. 5b shows the pHdependence of size-tunable PtCo alloys NPs. When the pH value becomes smaller, the surface of the support is more protonated. As a result, Pt and Co precursors have strong affinity to the support, resulting in the formation of small NPs. After atomic ordering through heat treatment, L10-PtCo NPs are formed, as characterized by XRD (Fig. 5c). The alternating layers of Pt and Co atoms could be observed in the TEM micrograph (Fig. 5d). The average size of these PtCo intermetallic NPs could be as small as sub-3 nm, meanwhile maintaining a narrow size distribution (Fig. 5e).

Electron-rich elements (S, N, O) that coordinate with Pt atoms are often incorporated into the carbon support to enhance the support-metal interaction.⁸⁹⁻⁹¹ Porous S-doped carbon (S-C) support was prepared by the cobalt-assisted carbonization of molecular precursors with silica NPs as the templates. 89,90 Metal salt precursors were impregnated onto the S-C supports with total metal content of 20 wt% and underwent high-temperature H2-reduction treatment to produce intermetallic NPs (Fig. 6a-c). Both L1₀-PtCo and L1₂-Pt₃Co intermetallic NPs could be produced using this method (Fig. 6d and e). The broad peaks in the XRD patterns suggest that these NPs have small crystal domains. Size analysis based on microscopic characterization further confirmed that the average size was typically less than 5 nm for these NPs (Fig. 6f and g). Instead of using premade S-doped carbon support, the S-C support could form in situ during the atomic ordering step under heat treatment. A molecule-assisted approach was reported for producing carbon supports doped with heteroatoms (S, N, O). 91 Molecular additives such as sodium thioglycolate (STG) were introduced into the mixture of carbon support and metal precursors. Heteroatom-doped graphene layers formed during the heat treatment and suppressed alloy sintering and particle growth of intermetallics. In general, enhanced support-metal interaction is effective in size control, though it could be detrimental for atomic ordering. For instance, the strong metal-S interaction suppressed not only the interparticle sintering but also intraparticle ordering, which restrained the formation of an ordered structure.89

3.4.2. Spatial confinement. Preventing atomic diffusion on surface may inhibit unwanted particle growth through confinement. The protective layer may be used, but it raises the concern that the layer itself may block active sites of intermetallic NPs. The removal of protective layers is often necessary to activate catalysts if such a strategy is used. 92,93 For example, 3 nm L1₀-PtCo intermetallic NPs can be synthesized via a surface coating strategy. 76,93 The dopamine coating was firstly introduced on the carbon-supported Pt NPs via π - π bond conjugation and subsequently converted into a carbon shell, resulting in the adsorption of Co ions. 93 Silica coating was then

Feature Article

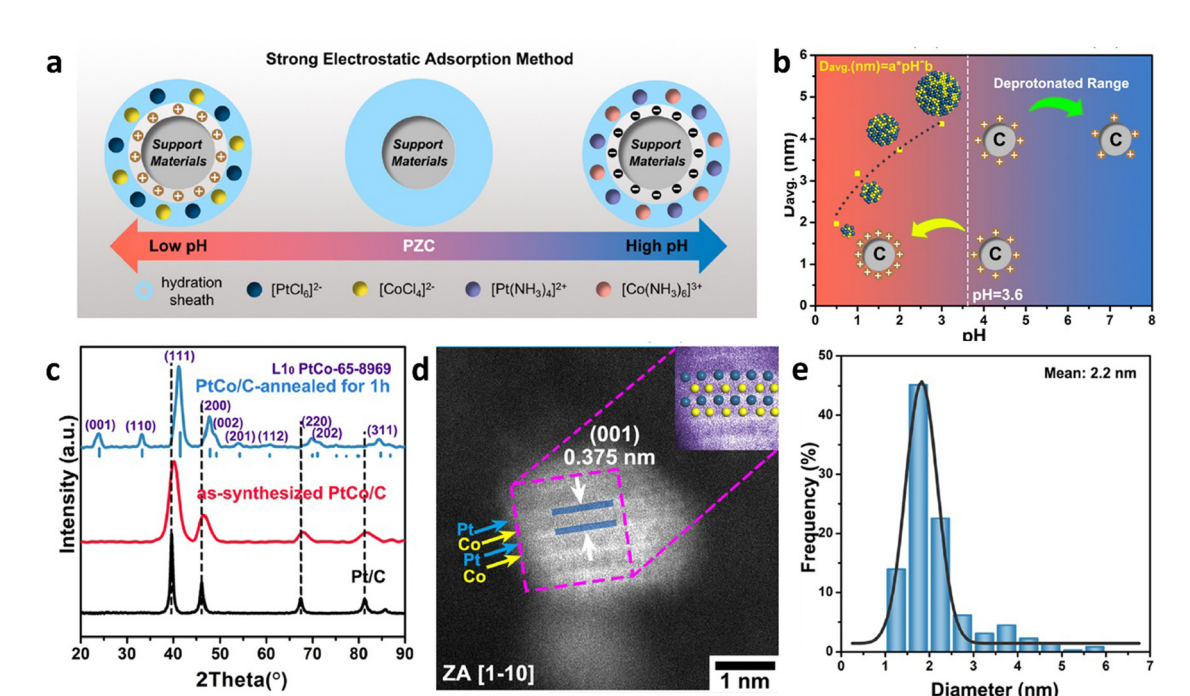


Fig. 5 (a) Schematic illustration of the SEA method for preparing bimetallic PtCo NPs on the N-doped carbon support in different pH ranges. A hydration sheath with the electrostatically adsorbed Pt and Co complexes formed on the surface by adjusting the pH value of the environment. (b) Illustration of effect of surface charges and the fitted curve of average diameter as a function of pH value of the A1-PtCo NPs. (c) XRD pattern, (d) HAADF-STEM image with a false-color enlargement (inset), and (e) size distribution analysis of the $L1_0$ phase intermetallic NPs. Reproduced with permission from ref. 59. Copyright 2021, Elsevier.

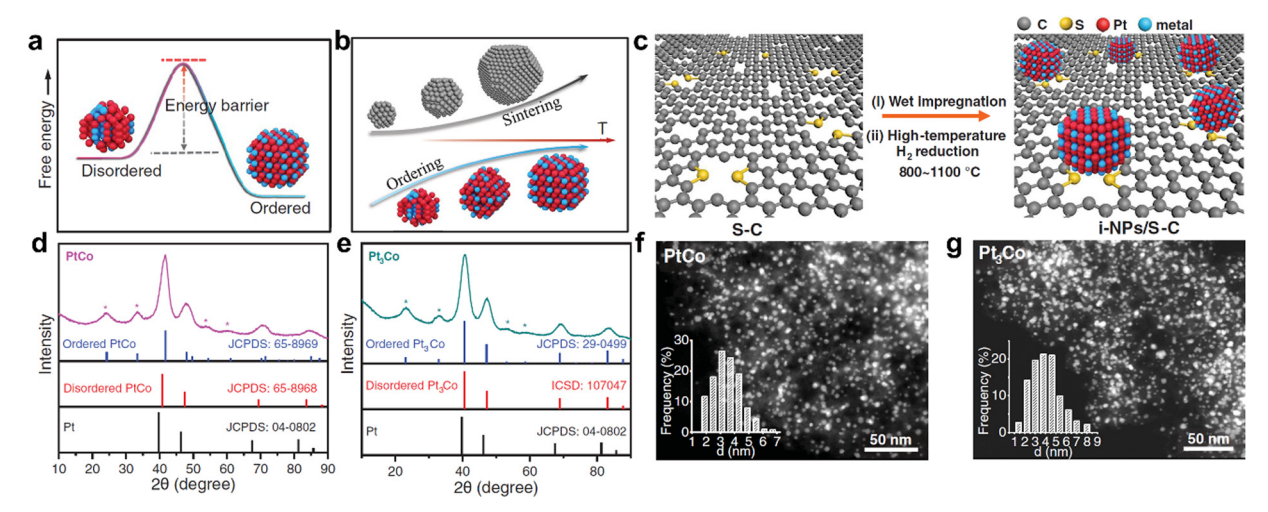


Fig. 6 Schematic illustrations showing (a) the kinetic energy barrier for atom ordering in the disorder-to-order transition, and (b) the trajectory in kinetics of simultaneously accelerated sintering and atom ordering with the change of temperature. (c) Schematic illustration of the high-temperature sulfur-anchoring approach. XRD patterns of (d) PtCo and (e) Pt3Co intermetallic NPs. The standard peaks for Pt and ordered and disordered PtCo/Pt3Co are also shown. Asterisks mark the characteristic peaks of ordered intermetallic structures. The HAADF-STEM images of (f) PtCo and (g) Pt3Co intermetallic NPs (inset: particle size distribution). Reproduced with permission from ref. 90. Copyright 2021, American Association for the Advancement of Science.

applied to the surface to prevent particle sintering during annealing. Such a rigid silica shell is effective in limiting the size growth but it also requires HF etching in the posttreatment steps. As a comparison, the carbon shell can be easily removed by air etching. 15,92

Other than protective layers, a certain support is capable of spatial confinement by itself. For example, the porosity of mesoporous carbon helps to control the particle size. 33,78,94 The synthesis procedures are generally similar to those of nonporous systems. Mesoporous carbon support is firstly obtained

ChemComm Feature Article

by the annealing of ZIF-8 or its derivatives. The metal precursors are impregnated onto the mesoporous carbon, and the mixture is dried either by heat treatment or freeze drying. ^{78,94,95}

3.5. Morphological control

The necessity for controlling the shape stems from the requirement for understanding the structure–property relationship to design electrocatalysts with high performance. For the catalytic property, the surface and near surface structures⁹⁶ of Pt-based bimetallic intermetallic NPs are particularly important. The surface structure and shape of Pt-Co intermetallic NPs are highly correlated since the shape of nanoparticle is determined thermodynamically by the surface energy and kinetically by the relative growth rates of different facets. In addition, the surface energy is affected by local environment and differs among different facets under different reaction systems. Low-index facets of crystals are often exposed due to their low surface energy and slow growth rate along their normal direction.

3.5.1. Shape and facet controls. Since most Pt–Co intermetallic NPs are produced by heat treatment, temperature is an important parameter to control the formation of exposed facets. The evolution of crystal facets could be studied by high resolution STEM. In the disorder-to-order transition of Pt₃Co alloy NPs, the $\{110\}$ planes were observed to be the main surface at 550 °C. When the temperature was raised to 600 °C, however, the $\{111\}$ facets became dominant and ultimately grew to 2–3 unit cell thick at 700 °C. As the temperature rose to 800 °C, the $\{110\}$ facets formed again, and the Pt₃Co intermetallic NPs evolved into a truncated cuboctahedra shape. Since surface faceting is closely related to the electrocatalytic properties, this work revealed that the preferred facets can be exposed with the judicious selection of processing temperature and other conditions.

Octahedral L1₀-PtCo NPs with {111} facets were often made by colloidal synthesis and subsequent annealing. 97 Pt-Co octahedral nanocrystals were firstly prepared in solution, followed by loading onto carbon supports. Atomic ordering was carried out in 4% H₂ at 600 °C to convert the alloy into L1₀-PtCo intermetallic. The formation of Pt skin was achieved by depositing excess Pt at 80 °C. The TEM micrograph shows that the octahedral nanocrystals have uniform size and exhibit welldefined {111} facets uniformly dispersed on the carbon support (Fig. 7a-c). The atomic resolution STEM image indicates that the nanoparticles were composed of a highly ordered L1₀-PtCo core with a smooth Pt shell of 3-4 atomic layers in thickness (Fig. 7d and e). To obtain the {111}-enclosed octahedral nanocrystal, the growth pattern of Pt was controlled by adjusting the reaction rate ratio between atom deposition and surface diffusion $(V_{\text{dep}}/V_{\text{diff}})$. The deposition of Pt atoms was initiated on the $\{001\}$ facets due to their higher surface energy than that of the {111} facets. The Pt adatoms may migrate to the edges and {111} facets through surface diffusion. When $V_{\rm dep}/V_{\rm diff} \ll 1$, the growth was dominated by surface diffusion, allowing a uniform coating of Pt and, ultimately, the formation of an octahedral L1₀-PtCo nanocrystal. The injection rate of precursors and reaction temperature can both affect the reaction rate ratio $(V_{\text{dep}}/V_{\text{diff}})$.

Synthesis of Pt-Co intermetallic nanostructures with highindex facets is non-trivial. The controlled synthesis of tetrahexahedral NPs is one of the few successful cases.⁵⁶ Density functional theory calculations show that surface modification by bismuth (Bi) stabilizes the {210} high-index facets and may result in tetrahexahedral NPs, regardless of their internal crystal structure. Without the modification by Bi, the specific surface energy is 1.70 J m⁻² for the {111} facet and 1.42 J m⁻² for the {001} facet. These values are smaller than those of the high-index facets (i.e., 2.27 J m⁻² for the {210} facet and 2.44 J m⁻² for the {201} facet), resulting in a truncated octahedron enclosed by {111}, {100}, {001}, and {101} facets, as suggested by Wulff theorem. Upon surface modification by Bi, the specific surface energy is expected to drop by $\sim 90\%$ for {210}, {102}, and {201} facets. Experimentally, pseudospherical PtCo alloy NPs successfully transformed into the L10 phase intermetallic with tetrahexahedral shape with {210} surfaces when they were annealed in Bi atmosphere.

While it is uncommon, one-dimensional nanowires consisting of L1₀-PtCo core⁹⁸ and Pt-rich surface were reported.²² This nanostructure exhibits compressively strained high-index facets. The preparation was carried out using platinum acetylacetonate (Pt(acac)₂) and Co(acac)₂ as metal precursors, along with cetyltrimethylammonium chloride (CTAC), glucose, oleylamine (OAm), and 1-octadecene (ODE). This mixture was treated with 5% H₂ at 550 °C for atomic ordering. The L1₀-PtCo nanowires maintained their one-dimensional morphology after this process (Fig. 7f). The green square in Fig. 7g corresponds to the enlarged region in Fig. 7h with the corresponding fast Fourier transform (FFT), suggesting high crystallinity. The homogeneity of elemental distribution was demonstrated by EDX elemental maps (Fig. 7i). The analysis of the interplanar distance and the stepped atomic terminations suggested that the edges of the annealed nanowires possessed the high-index facets {221} and {211} (Fig. 7j). The formation of nanowires required the presence of both glucose and CTAC. The surface became smooth when CTAC was replaced with cetyltrimethylammonium bromide (CTAB). This observation indicates that the choice of halide played a role in the formation of high-index facets. Such a one-dimensional structure provides high contact area with the carbon support and requires no protective layer to prevent agglomeration during annealing. In this context, the nanowires seem to be thermally stable. The annealed nanowire formed a thin Pt-rich layer, which enhanced its durability as electrocatalysts. Besides the L10 phase, L12-Pt3Co nanowires were prepared via nanometer (nm)-sized spatial confinement using mesoporous silica templates.99 The porous templates allow control over the size and shape of the nanostructures and prevent agglomeration during the atomic ordering process at a high temperature. The as-prepared Pt₃Co intermetallic nanowires were catalytically active in both alkaline hydrogen evolution reaction and acidic methanol oxidation reaction.

3.5.2. Core-shell structure. Pt-Co intermetallic NPs often exist or are made in core-shell structures, typically with the Pt shell. Molecular dynamics simulations were carried out to compare the thermo-stability of Pt- and Co-coated

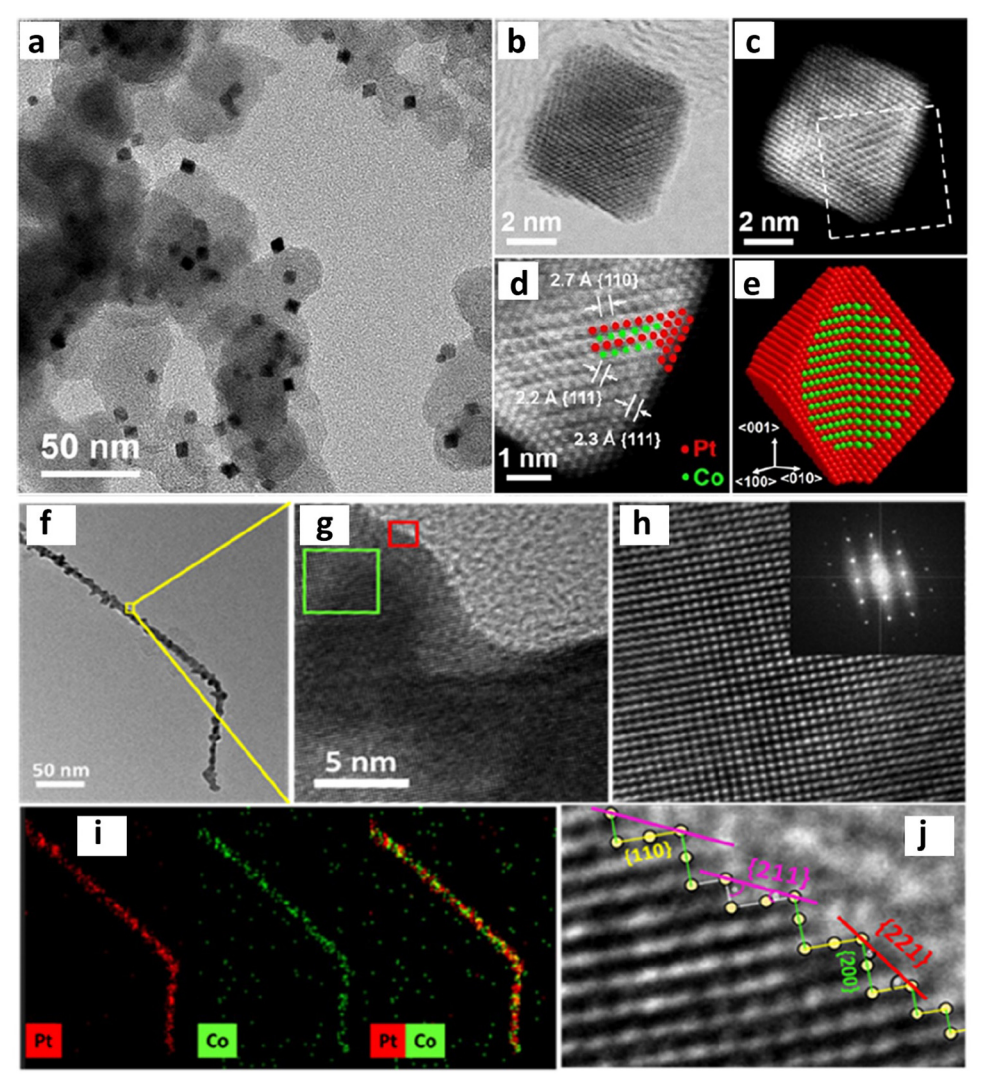


Fig. 7 Characterization of the fct PtCo@Pt octahedral nanocrystals supported on carbon. (a) TEM image, (b) high-angle annular bright field-, and (c) HAADF-STEM images of a nanocrystal along the [1–10] direction. (d) Atomic-resolution STEM image taken from the corner region marked by a box in panel (c). (e) Schematic of the nanocrystal featuring an intermetallic core, a Pt shell of about three atomic layers thick, and {111} facets. Reproduced with permission from ref. 97. Copyright 2021, American Chemical Society. (f) TEM image of PtCo/C NW annealed at 550 °C, (g) the corresponding HR-TEM image, (h) HR-TEM image, and the FFT (inset) of the green box region in (g). (i) EDS elemental mapping and (j) HR-TEM image of the red box region in (g). Reproduced with permission from ref. 22. Copyright 2022, American Chemical Society.

L₁₂-Pt₃Co NPs. ¹⁰⁵ The simulated results suggest that Pt is much better than Co as the coating element for improving both the structural and thermal stability of Pt₃Co NPs. Platinum shell was often observable directly using high resolution STEM.²⁸ Typically, such a Pt shell contains 2 to 3 atomic layers and was strained by the ordered L12-Pt3Co intermetallic core. Such coreshell structures could exhibit better durability than the alloys after potential cycling between +0.05 and +1.00 V for 5 k cycles in 0.1 M HClO₄ solution. During the cycling, surface roughening and removal of contaminants could result in high electrochemical surface area (ECSA) in a short time, but only those NPs consisting of well-ordered Pt shell and L12-Pt3Co intermetallic core possessed long-term stability in ECSA.

The mechanism for the formation of Pt skin may vary as the behavior of surface atoms change under different heat treatments in the atomic ordering step. Aberration-corrected environmental TEM was used to examine the surface evolution of Pt-Co bimetallic NPs during the oxidation in O2 and reduction in H₂ processes.³¹ Under oxidation conditions, Co atoms could migrate to the surface to form a strained oxide layer. The surface strain was relaxed through the formation of Co oxide islands afterward. Co atoms could move back to the core during the reduction, resulting in the formation of Pt monolayer on the surface.

In another case, when the atomic ordering of Pt₃Co NPs took place in O₂, the L1₂-Pt₃Co intermetallic formed, together with Pt surface segregation during the disorder-to-order transition (Fig. 8a and b).²⁹ HR-STEM false color image shows the atomic structures of the {100} surface (Fig. 8a, red box region). Two atomic layers of Pt, instead of a monolayer, were observed on

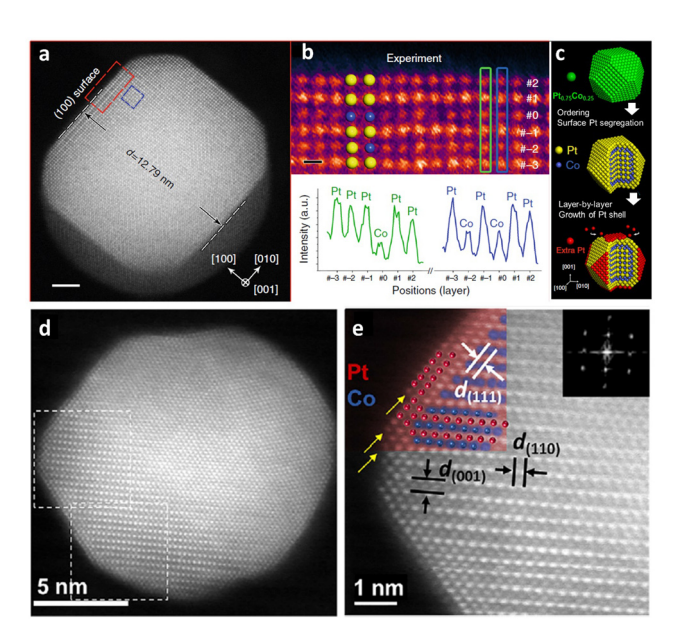


Fig. 8 (a) In situ HAADF-STEM image showing a Pt₃Co NP after being exposed to oxygen for 30 min at 720 °C (scale bar: 2 nm). (b) Enlarged false color image of the (100) surface in the red box in (a), and the intensity profiles taken along the atomic layers marked by green and blue rectangles, showing the segregated Pt-rich surface (scale bar: 2 Å). (c) Schematic diagrams showing the process of the oxygen-driven formation of coreshell structure in Pt₃Co NPs. Reproduced with permission from ref. 29. Copyright 2017, Nature Publishing Group. (d) The STEM image of L1₀-PtCo/Pt NPs with 2-3 atomic layers of Pt shell on the L1₀-PtCo core (dark atom is Pt and light atom is Co), zone axis is $\langle 1-10 \rangle$ direction. (e) Enlarged section indicated by the top dashed square in (d), showing the 2-3 atomic layers of Pt shell (indicated by yellow arrows) and the L1₀-PtCo core (red-Pt, blue-Co). Reproduced with permission from ref. 30. Copyright 2019, Cell Press.

the {100} surface (Fig. 8b). Such surface segregation of Pt effectively prevented the oxidation of Co. When the temperature was decreased to 300 °C, Pt atoms from other clusters migrated and attached on the {100} facet of the L12-Pt3Co NPs, giving rise to a layer-by-layer growth of the Pt shell in oxygen atmosphere (Fig. 8c).

Acid treatment could result in the formation of Pt shell with more than two atomic layers on the intermetallic core (Fig. 8d and e). 30 The fully ordered L10-PtCo NPs could form such coreshell structures after they were treated in 0.1 M HClO₄ at 60 °C in air for 24 h, followed by annealing under 5% H₂ in Ar at 400 °C for 2 h. The STEM micrograph shows that the core-shell structure was formed, with the core consisting of alternative layers of Pt and Co and the shell being 2-3 atomic thick of Pt. Such a core-shell structure is efficient in protecting Co against acid etching.

Besides the above case studies where Pt atom was used, carbon^{76,93} and ionic liquids¹⁰⁶ were also used to make the shell. For example, dopamine was used to coat the carbonsupported Pt NPs and subsequently converted into nitrogendoped carbon shell via pyrolysis under H₂ atmosphere. 93 Interestingly, even if Pt atoms were covered, enhanced catalyst durability was observed with a high ORR mass activity of 1.36 mA mg_{Pt}^{-1} .

4. Selective recent examples for the preparation of Pt-Co intermetallic NPs

Platinum-cobalt alloy NPs or their metal ions on catalyst support are usually converted into intermetallic structures through heat treatment because this approach greatly reduces atomic diffusion length for the formation of intermetallic. Furthermore, a low-temperature atomic ordering process is preferable to reduce the possibility of particle sintering and coalescence. There are two main steps in a typical synthesis of intermetallic NPs—preparation of alloys or metal ion intermediates as precursors and conversion to intermetallic through atomic ordering. The second step is normally conducted using heat treatment in reductive gas atmosphere, though a microwave-induced ordering is also reported. 107 In this feature article, we categorize the current methods for the synthesis of Pt-Co intermetallic NPs based on the initial step and summarize them in Table 1.

Colloidal synthesis is a popular method for preparing faceted, metal alloy NPs because the added surfactants can be adsorbed on certain metal facets (i.e., {hkl}) and often slow down the growth rate in the corresponding [hkl] direction. Such solution phase synthesis has the advantage of easy control over the structure parameters of the formed NPs. 108 The surfactants used may be adsorbed on crystal surfaces and block the catalytic active sites, although they can be removed during the heat treatment. For example, in the preparation of carbonsupported L10-PtCo NPs, PtCo alloy NPs were firstly prepared using Pt(acac)₂, Co(acac)₂, and OAm via colloidal synthesis.³⁰ OAm served as both solvent and reducing agent. The as-prepared alloy NPs were dispersed on carbon to prepare the intermetallic after being treated in 5% H₂ at 650 °C for 6 h.

Impregnation is a common method for preparing Pt-Co intermetallic NPs. In this approach, metal precursors dissolve in aqueous or organic solvents and are loaded subsequently onto supports, typically made of various types of carbon. The optimal volume of solvent is around the pore volume of the support; thus, capillary force may draw solution into pores, resulting in the uniform dispersion of metal precursors. Solvents are then removed by either heating or freeze drying. The solid products go through atomic ordering to produce intermetallic NPs. The metal precursors may be reduced directly to intermetallic compounds or form alloys first and then go through disorder-to-order transition.⁵⁹ Depending on compositions and other structural factors, it may take more than one heating step to obtain the final products.91 The detailed change of atomic restructuring process remain a difficult subject to study because of the limitation of in situ characterization. Vulcan XC-72 and Ketjen black are the commonly used carbon supports. Mesoporous functionalized carbon made from pyrolysis of zeolitic imidazolate framework (e.g., ZIF-8 and ZIF-67) was also reported. 78,94,109 Certain ZIF-derived carbon may function as the host structure for Co due to the atomically dispersive capability of metal species.110 Heteroatoms are often incorporated into the carbons support and help to enhance support-metal interaction, thus achieving better size control. 90,91

This journal is © The Royal Society of Chemistry 2023

Table 1 Synthesis procedures of selected Pt–Co intermetallic nanostructures

Composition	Intermetallic structure	Precursor	Support (spec), additive	e	Processing condition for ordered phase	Ref.
W-doped PtCo	L1 ₀	Pt(acac) ₂ , Co(acac) ₂	Carbon (Vulcan XC-72), OAc, OAm		400 °C, 1 h (5% H ₂ /Ar)	80
PtCo	$L1_0$	$Pt(acac)_2$, $Co(acac)_2$,	Carbon (Vulcan XC-72)		600 °C, 4 h (4% H ₂ /Ar)	97
PtCo	L1 ₀	$Pt(acac)_2$, $Co(acac)_2$,	Carbon (Ketjen-300J), C	JAM ————————————————————————————————————	650 °C, 6 h (5% H ₂ /Ar)	30
Impregnation-ba	sed synthesis					
Composition	Intermetallic structure	Precursor	Support (spec)	Processing co	ondition for ordered phase	Ref.
PtCo	L1 ₂	H ₂ PtCl ₆ , CoCl ₂	Carbon (Vulcan XC-72)	650 °C, 4 h (1	10% H ₂ /N ₂)	95
PtCo	$L1_0$	H_2 PtCl ₆ , $C_{16}H_{40}$ Cl ₄ CoN ₂	Carbon (N-doped) 700 °C, 1 h (va		,	59
PtCo	$L1_0$	H ₂ PtCl ₆ , Co(NO ₃) ₂	Carbon (N-doped) 700 °C, 2 h (H_2			88
$PtCo_{1-x}Ni_x$	L1 ₀	H ₂ PtCl ₆ , CoCl ₂ , NiCl ₂	Carbon (Vulcan XC-72)	700 °C, 2 h (1		77
Pt_3Co $PtCo_{1-x}Cu_x$	$egin{array}{c} ext{L1}_2 \ ext{L1}_0 \end{array}$	H ₂ PtCl ₆ , CoCl ₂ H ₂ PtCl ₆ , CoCl ₂ , Cu(NO ₃) ₂	Carbon (Vulcan XC-72) Carbon (EC-300J)	700 °C, 2 h (1 700 °C, 2 h (5		28 81
N-doped Pt ₃ Co	L1 ₀ L1 ₂	H ₂ PtCl ₆ , CoCl ₂ , Cu(NO ₃) ₂ H ₂ PtCl ₆ , CoCl ₂	Carbon (Vulcan XC-72)	700 °C, 2 h (1		113
Pt ₃ Co	$L1_2$ $L1_2$	H ₂ PtCl ₆ , CoCl ₂	Carbonized ZIF-8	750 °C, 2 h (8		94
Pt ₃ Co _{0.6} Ti _{0.4}	L1 ₂	H ₂ PtCl ₆ , CoCl ₂ , TiCl ₃	Carbonized ZIF-8	750 °C, 2 h (I		78
PtCo	$L1_0$	H ₂ PtCl ₆ , CoCl ₂	Carbon (Ketjen black)	800 °C, 2 h (5		33
Pt ₃ Co	$L1_2$	H ₂ PtCl ₆ , CoCl ₂	Carbon (Ketjen black)	800 °C, 2 h (5	5% H ₂ /Ar)	33
PtCo	$L1_0$	H_2PtCl_6	Bimetallic MOF Zn _x Co _y -derived carbon materials	900 °C, 2 h (5	5% H ₂ /Ar)	109
PtCo	$L1_0$	H ₂ PtCl ₆ , CoCl ₂	Carbon black	900 °C, 2 h (1	H_2), followed by 600 °C, 6 h (H_2)	91
Pt ₃ Co	$L1_2$	H_2 PtCl ₆ , Co(NO ₃) ₂	Carbon (S-doped)		5% H ₂ /Ar), followed	90
Co-reduction				by 000 C, 0	(370 119/14)	
	Intermetallic				Processing condition for	
Composition	structure	Precursor	Support (spec), reductant		ordered phase	Ref.
Pt ₃ Co	$L1_2$	H ₂ PtCl ₆ , CoCl ₂ K ₂ PtCl ₄ , HAuCl ₄ , Co(HC	Carbon (Vulcan X OO) ₂ Carbon (Vulcan X		600 °C, 2 h (H ₂) 700 or 800 °C, 0.5 h (H ₂ /Ar)	99 111
Au ₁₀ Pt ₄₀ Co ₅₀ Surface coating	L1 ₀	K ₂ PtCl ₄ , HAuCl ₄ , Co(HC	Carbon (vuican X	С-72], Nавп ₄	700 01 800 C, 0.3 II (H ₂ /AI)	111
Burrace coating						
Composition	Intermetallic structure	Precursor	Additive		Processing condition for ordered phase	Ref.
PtCo	L1 ₀	Pt/C , $Co(NO_3)_2$	Dopamine, tetraethyl orthosilicate		800 °C, 2 h (10% H ₂ /N ₂)	93
Pt ₃ Co	L1 ₂	H ₂ PtCl ₆ , CoCl ₂	Polydopamine, carbon (Vu	alcan XC-72)	900 °C, 0.5 h (Ar)	92
Template-assiste	d synthesis					
Composition	Intermet structure		Template	;	Processing condition for ordered phase	Ref.
Pt ₃ Co	$L1_2$	H ₂ PtCl ₆ , Co	Silica (SBA-15)		600 °C, 2 h (H ₂)	99
PtCo	$L1_0$	H ₂ PtCl ₆ , Co			700 °C, 2 h (H ₂ /Ar)	76
Pt ₃ Co	L1 ₂	H ₂ PtCl ₆ , Co	(NO ₃) ₂ NaCl, glu	cose	790 °C, 2 h (5% H ₂ /Ar)	112
Other methods						
Composition	Intermetallic structure	Precursor	Additive		Processing condition for ordered phase	Ref.
PtCo	$L1_2$	K ₂ PtCl ₄ , Co(NO ₃) ₂ ,	_		600 °C, 3 h (5% H ₂ /Ar)	114
PtCo	$L1_0$	2-methylimidazole $Co(CH_3COO)_2$, K_2PtCl_4	Carbon (Ketjen l (Vulcan XC-72)	olack) or carbon	600 °C, 24 h (Ar)	115
PtCo ₃	$L1_2$	H_2 PtCl ₆ , Co(NO ₃) ₂	Polyvinyl pyrrolic (Vulcan XC-72)	done, carbon	600 or 700 °C, 2 h (H ₂)	55
PtCo	$L1_0$	H ₂ PtCl ₆ , CoCl ₂	Ionic liquid, carl	on black	700 °C, 2 h (N ₂)	106
Pt ₃ Co	$L1_2$	H_2PtCl_6 , $CoCl_2$	Carbon (Vulcan	XC-72)	700 °C, 2 h (H ₂ /N ₂)	102
PtCo	$L1_0$	H_2PtCl_6 , $Co(NO_3)_2$	NH ₃ ·H ₂ O, carbon	n (Vulcan XC-72)		104
PtCo	L1 ₀	K_2PtCl_4 , $K_3Co(CN)_6$,	_		700 °C, 68 h (Ar)	116
Pt ₃ Co	$L1_2$	K_2 PtCl ₄ , K_3 Co(CN) ₆ , Co			750 °C, 2 h (Ar)	116
Pt ₃ Co	$L1_2$	H_2PtCl_6 ,	Co-doped ZIF de	riveu carbon	900 °C, 0.5 h (vacuum)	110
Cu-doped PtCo	$L1_0$	Pt(acac) ₂ , Cu(acac) ₂ , Co	₂ (CO) ₈ Carbon (Vulcan 2	XC-72)	Microwave, 1200 W, 30 s,	107

ChemComm Feature Article

Co-reduction is used to produce Pt and Co metal species, or more specifically, Pt-Co alloys, from the corresponding salt precursors in liquid. In this case, reducing agents such as sodium borohydride (NaBH₄) is required. ^{99,111} For example, Co could be introduced first through the reduction of its salt by NaBH₄ in aqueous solution. A mixture of K₂PtCl₆ and HAuCl₄ was then added to the aqueous solution and sonicated to obtain AuPtCo alloy core-shell NPs. 111 After atomic ordering via heat treatment, L1₀-Au₁₀Pt₄₀Co₅₀ core-shell half-intermetallic NPs were

Surface coating and template-assisted syntheses are often conducted to produce specific nanostructures. Dopamine was applied as the surface coating molecule to synthesize L1₀-PtCo intermetallic NPs with a nitrogen-doped carbon shell that protects L1₀-PtCo from metal leaching in the electrochemical processes.⁹³ Dopamine was also used to form a polymeric surface around the NPs against particle growth in the heat treatment steps. 92 As for template-assisted synthesis, template is used to either produce intermetallic with controlled morphology⁹⁹ or control the structure of carbon support.¹¹²

In general, there is a tradeoff in the synthesis of Pt-Co intermetallic NPs for optimal electrocatalytic performance. The choice of temperature and heating profile is often crucial for producing an intermetallic structure. High temperature is beneficial for facilitating atomic diffusion and increasing the crystallinity, though it may result in an increase in both size and size distribution because both particle sintering and Ostwald ripening may occur under such processing conditions. Inversely, low temperature process may be good for size control, but it suffers from a low degree of ordering. In addition, surfactants and excess surface carbon may not be removed at low synthesis temperatures. Similarly, incorporation of a protective layer such as carbon shells needs to balance the size control and deactivation or blocking of surface active sites. The enhanced support-metal interaction is effective in inhibiting atomic diffusion and particle migration in the disorder-to-order transition, though the energy barrier for atomic ordering may increase. Loading amount of metal precursors should be controlled. Low loading is preferred for the highly uniform dispersion of intermetallic NPs, but it increases the average atomic diffusion length during the ordering process and reduces the packing density of catalyst NPs. Thus, controlled experiments and optimization are necessary to map out the effects of different conditions for the preparation of highly ordered, size-controlled Pt-Co intermetallic NPs.

5. Application of Pt-Co intermetallic NPs in electrocatalysis

Many Pt-M (M = Co, Fe, Ni) bimetallic materials are theoretically predicted to possess better ORR activity than pure Pt NPs. 9,26,27,117 However, electrocatalysts consisting of Pt-Fe species suffer from the Fenton reaction, where ferrous and ferric cations can catalyze the formation of oxidizing agents from H2O2, accelerating the degradation of electrocatalysts or decomposition of fuel cell components (e.g., Nafion

membrane). Electrocatalysts made from Pt-Ni alloys exhibit high ORR activity, 18,118,119 though they may be harder to synthesize and less stable than Pt-Co. In this context, electrocatalysts consisting of Pt-Co alloy NPs attract much attention, especially after its use in commercial fuel cell systems. 40 With the need for heavy-duty applications, 13 addressing the challenge of durability becomes increasingly critical.

Pt-based intermetallic NPs, in this regard, often exhibit better stability than their alloy counterparts. 105,120-122 The ORR stability may be attributed to the strong bonding between Pt and the other metal, which results in a more negative enthalpy of formation. 43,44 Intermetallics often exhibit less metal dissolution, less ECSA loss, and better durability than their alloy forms under the same reaction conditions. 123,124 Furthermore, there is an ease in analyzing the composition of the near-surface region of intermetallic structures, 43,96 which help to develop more reliable surface models in the theoretical calculation of adsorption 111,125,126 and the mechanism study of a catalyst. 78,80,117 In this section, we discuss the correlation between the structural features and catalytic properties of Pt-Co intermetallic electrocatalysts, i.e., activity and durability.

Briefly, there are two major experimental approaches for the characterization of electrocatalysts—the three-electrode system based on rotating disk electrode (RDE) technique and the full cell study using membrane electrode assembly (MEA). The RDE test is primarily based on the analysis of polarization curve obtained from linear scanning voltammetry (LSV). The value of current density under different potentials (vs. reversible hydrogen electrode, RHE) is frequently used to compare the performance in the kinetically controlled regime because the RDE technique can greatly reduce mass transfer resistance. Mass activity in A mg_{Pt}⁻¹ obtained from the polarization curve at 0.9 V (vs. RHE) is a common parameter for comparing the ORR activity. When other precious metal (e.g., Pd) is incorporated, the mass of all noble metals should be included besides Pt, partly because of the economic consideration of the scale-up production of PEMFCs. Area specific activity (or specific activity) is used to compare the intrinsic activity based on the electroactive metal site. In the latter case, the value of surface area is obtained based on the ECSA measurement, which is an estimation of Pt (or Pd) metal sites calculated based on the {111} surface and should be distinguished from the geometric surface area. For durability, accelerated stress test (AST) is a primary testing method where an applied potential continuously cycles in the predetermined potential window. Mass activity is reported at the beginning of life (BOL) and the end of life (EOL, usually 30 k cycles). The percentage retention of mass activity quantitatively describes durability. Table 2 summarizes the RDE-based ORR performance data of Pt-Co intermetallic electrocatalysts reported in recent years based on the activity and durability metrics.

Noticeably, RDE-based measurements focus on optimizing the testing conditions to reduce the mass transfer resistance and other factors for obtaining the highest kinetic current density data. As the catalytic test takes place in liquid using the RDE technique while the MEA-based single cell study operates under different levels of humidity, the ORR performance

Feature Article

Table 2 Summary of ORR catalytic performance before and after AST for selected Pt-Co intermetallic catalysts based on RDE measurement^a

Catalyst			Mass activity @ 0.9 V (A mg _{Pt} ⁻¹)			
Name	Core@shell	Intermetallic structure	BOL	EOL	Durability (%) (test condition)	Ref.
PtCo@Pt	Pt-shell	L1 ₀	0.48	0.38	80 (60 k, 0.6-1.0 V)	109
O-PtCo ₃ @HNCS	Carbon shell	$L1_0$	0.54	0.50	92.6 (20 k, 0.6-1.0 V)	76
L1 ₀ -PtCo/C	_	$L1_0$	0.67	0.64	96.7 (10 k, 0.6–1.0 V)	59
AuPtCo/C-700	Pt shell	$L1_0$	0.68	0.66	97.1 (10 k, 0.6–1.0 V)	111
PtCo/C-600	Pt shell	$L1_2$	0.68	0.51	74.9 (30 k, 0.6–1.0 V)	95
Pt-Co-Mo	Pt shell	$L1_0$	0.89	0.62	70 (30 k, 0.6–1.0 V)	126
fct-PtCo/C@ILs	Ionic liquid shell	$L1_0$	1.04	0.94	90.4 (10 k, 0.6-1.1 V)	106
L1 ₀ -PtCo	_	$L1_0$	1.27	0.80	63 (30 k, 0.6-1.1 V)	88
PtCo@NC-60	Carbon shell	$L1_0$	1.36	1.26	93 (20 k, 0.6–1.2 V)	93
$Pt_3Co_{0.6}Ti_{0.4}$	Pt-shell	$L1_2$	1.49	1.19	79.9 (20 k, 0.6–1.05 V)	78
L1 ₀ -W-PtCo/C	Pt shell	$L1_0$	2.21	2.04	92.3 (10 k, 0.6-1.0 V)	80
L1 ₀ -CoPt	Pt shell	$L1_0$	2.26	1.83	81.0 (30 k, 0.6–1.0 V)	30
fct-Pt-Co@Pt/C	Pt shell	$L1_0$	2.82	2.23	79.1 (30 k, 0.6–1.1 V)	97
L1 ₀ -CoNiPt	Pt shell	$L1_0$	3.1	2.6	84 (30 k, 0.6-1.0 V)	117

^a The value of durability is the retention of mass activity at 0.9 V (vs. RHE), which is obtained or estimated from the reported polarization curves. Numbers in the parentheses represent the numbers of AST cycles and the corresponding potential window. Only intermetallic catalysts with no less than 10 k AST cycles are listed in Table 2. The values of EOL mass activities in Table 2 are calculated based on the reported BOL mass activities and retention rates if they are not explicitly reported in the referred publications.

data cannot be compared directly between these two types of measurements.88,104 The discrepancy between RDE and MEA results is often quite large and can be attributed to multiple factors. Mass transfer resistance is often much higher in the MEA test than in the RDE-based measurement. In addition, the MEA tests are usually performed under high metal loading, elevated temperature, and with different backpressure and humidity, using both air and pure oxygen in MEA stack. 127 All of these conditions affect the catalytic performance. In addition, the leaching of non-Pt metal could corrode the MEA. In this context, MEA measurement becomes increasingly important, especially in the development of PtCo-based NP electrocatalysts designed for durable PEMFC systems toward heavy-duty applications.

The typical MEA-based assessments of catalytic performance share a few common features with those of RDE tests. In a widely used AST protocol, the mass activity at the cell voltage of 0.9 V is measured before and after 30 000 times of square wave cycles between 0.6 and 0.95 V. While there exist other electrochemical stability test protocols such as pulse cycling methods,

the aforementioned AST method can simulate material degradation in the MEA under the operating conditions over a much shorter time frame than the rest.38 The potential loss at 0.8 A cm⁻² is important for the AST and reported from the polarization curves after predetermined numbers of cycles (i.e., 1 k, 5 k, 10 k, and 30 k), together with the percentage loss in ECSA.37 There are fewer reports on the MEA-based ORR performance of Pt-Co intermetallic electrocatalysts because of multiple reasons, which include difficulty in preparing highquality MEA reproducibly, uncontrollable variation in the testing conditions, and differences in the testing protocol. Table 3 summarizes a selection of recently reported MEA results using the suggested metrics to compare the results under the same or comparable conditions.

The degree of ordering of the intermetallic Pt-Co electrocatalyst was found to correlate well with the ORR activity, 60,71,84,85,129 and a higher degree of ordering results in higher activity. 61 The incorporation of a third metal into the Pt-Co intermetallic system (i.e., mixed-element half-intermetallic) helped change the Pt-Pt

Table 3 Summary of the ORR catalytic performance for state-of-the-art Pt-Co intermetallic catalysts based on the MEA measurement

	Catalyst	Mass activity @ 0.9 V (cell voltage)			Loss in potential (mV)		
Gas type		BOL (A mg _{Pt} ⁻¹)	EOL (A mg _{Pt} ⁻¹)	Retention (%)	(@ a given current density in A cm $^{-2}$)	Loss in ECSA (%) (number of AST cycles)	Ref.
H ₂ -O ₂	L1 ₀ -CoPt	0.56	0.45	81	_	12.9 (30 k)	30
2 2	L1 ₀ -W-PtCo/C	0.57	0.47	82.5	_	_ ` ´	80
	L1 ₀ -CoPt@Pt-shell	0.60	0.36	60	_	_	122
	Sub-Pt ₃ Co-MC	0.92	0.81	87.8	_	_	33
	PtCo i-NPs	1.52	1.17	77	_	_	90
H ₂ -air	Pt ₃ Co/C-750	0.5	0.4	80	20 (2)	27 (30 k)	61
	PtCo/KB-NH ₂	0.691	0.380	55.0	30 (0.8)	_ ` ′	128
	Pt ₃ Co/FeN ₄ -C	0.72	0.441	38	23 (1.0) 21 (0.8)	_	125
	STG-assisted PtCo	1.08	0.81	75	21 (0.8)	_	91
	Pt ₃ Co/DMC-F	_	_	_		20.9 (10 k) 30 (20 k)	94
	$Pt_3Co_{0.6}Ti_{0.4}$	_	_	_	_	19.8 (30 k)	78
	L1 ₀ -CoPt@Pt-shell	_	_	_	26 (0.8)	33 (30 k)	122

ChemComm Feature Article

distance to optimize the binding energy between surface Pt atoms and O intermediates. 78,80,81 The surface of L10-PtCo NPs modified by Mo-Ox species (Fig. 9a and b) could exhibit a weakened binding energy of the oxygen species on Pt (Fig. 9c and d), resulting in an enhancement in the ORR performance under both RDE and MEA testing conditions. 126 Single atoms of Co-N-C support may change the binding energy between the oxygen species and Pt surface, whereas direct electron transfer from PtCo to the Co-N-C support could result in the d-band shift of Pt. 130,131

The incorporation of metal into the Pt-Co lattice may change the surface strain and enhance the ORR activity. 117 An eigenforce model was constructed to predict the straininduced enhancement of the ORR activity (Fig. 9e). This model was used to analyze the ORR performance based on two popular mechanisms: associative, in which the O-O bond stays intact upon adsorption and protonation (Fig. 9f), and dissociative, in which the O-O bond is broken upon adsorption (Fig. 9g). The underlying principle is that the change in the subdomain of an extended surface may result in eigenstress on the surface boundary. The adsorbed oxygen species may cause either the attraction or repulsion of the neighboring metal atoms. Understanding the interplay between applied strain and the induced eigenstress helps to predict the effect of strain on the binding of adsorbates. A 2D volcano plot could be created to locate the optimal ternary NPs by calculating the binding energy of Pt surfaces of different L1₀-PtCo_{0.5}M_{0.5} (M = Mn, Fe, Ni, Cu, Ni) (Fig. 9f and g). This theoretical screening guided the synthesis of the L1₀-PtCoNi NP electrocatalyst,

which exhibited a mass activity of 3.1 A mg_{Pt}⁻¹ and a specific activity of 9.3 mA cm⁻² at 0.9 V (vs. RHE). The RDE-based AST showed a 15.9% loss of mass activity after 30 k cycles at 60 °C in 0.1 M HClO₄.

Size control plays an important role in improving the ORR activity of PtCo intermetallic electrocatalysts. 33,59,88,90,94 Fig. 10 shows the ORR activity and durability studies of sub-3 nm L₁₀-PtCo NPs supported on nitrogen-doped carbon.⁵⁹ The strong electrostatic adsorption of metal species on functionalized carbon helped in suppressing particle sintering during the heat treatment. Such PtCo intermetallic electrocatalyst exhibited a half-wave potential 64 mV higher than that of the Pt/C (Fig. 10a). Both the mass and specific activities of intermetallic PtCo electrocatalysts were significantly higher than Pt/C and fcc PtCo random alloy phase in RDE tests (Fig. 10b). Moreover, the PtCo intermetallic electrocatalyst, which had the highest activity among the three, exhibited only a 3.3% drop in the mass activity after 10 k of RDE-based AST cycles. The mass activity dropped by 30% for the PtCo random alloy catalyst tested under the same conditions (Fig. 10c). Such a study demonstrates the advantages in both the activity and durability of using PtCo intermetallic NPs as ORR electrocatalysts.

The shape of the Pt-Co intermetallic NPs can be an important structural factor for the ORR performance since lattice mismatch between the intermetallic core and the Pt shell¹⁰¹ results in different levels of induced strain based on the exposed surfaces. 109,132 Such strain effect and ligand effect were studied by theoretical calculations. 99,117 Subsized L12-Pt3Co

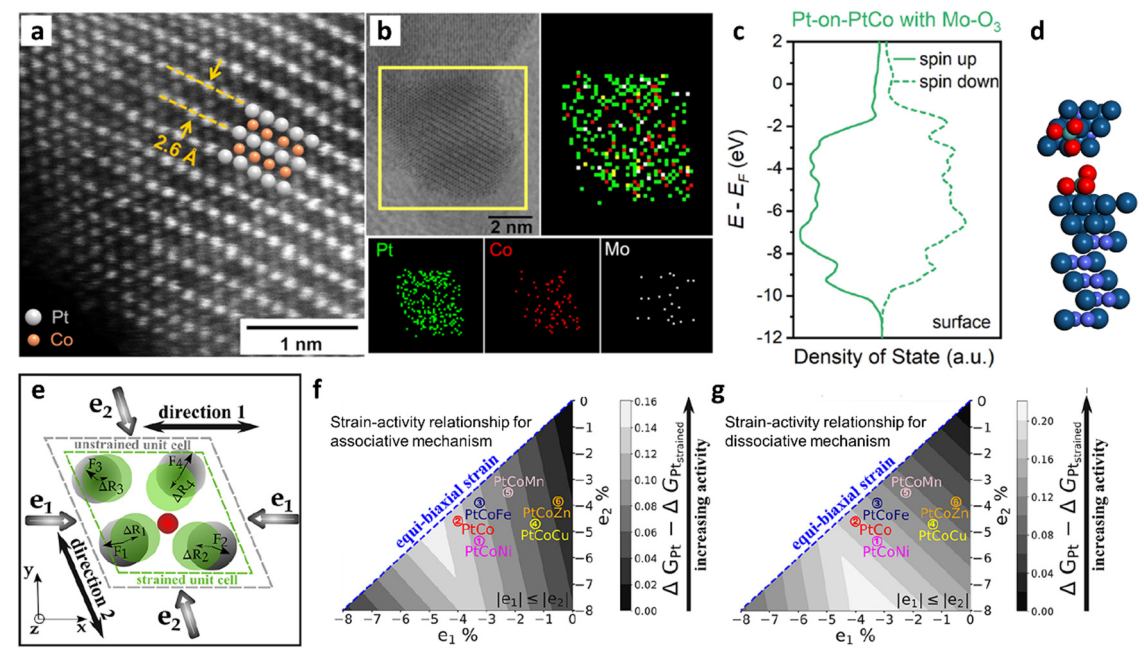


Fig. 9 (a) High-resolution HAADF-STEM micrograph showing the intermetallic features of the Pt-Co-Mo electrocatalyst. (b) HAADF-STEM EDS map showing the Pt, Co, Mo distribution of the catalyst particle in (a). (c) Calculated density of states of the d-orbitals of the surface Pt, and (d) top/side view of Pt-on-PtCo with Mo-O₃ structures. Reproduced with permission from ref. 126. Copyright 2022, Elsevier. (e) Illustration of the in-plane components of the adsorbate-induced eigenforces and the displacement caused by an applied strain. Calculated 2D volcano plots of the strained Pt (111) surfaces using the eigenforce model for (f) the associative mechanism and (g) the dissociative mechanism. Reproduced with permission from ref. 117. Copyright 2020, American Chemical Society

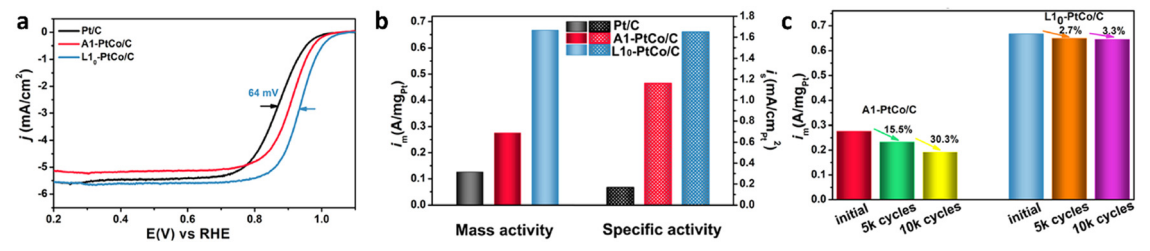


Fig. 10 (a) ORR polarization curves, (b) mass- and area-specific activities at 0.9 V (vs. RHE), and (c) mass activity for the initial, 5 k, and 10 k CV cycles for the sub-3 nm ordered intermetallic L1₀-phase PtCo/C electrocatalysts, respectively. Reproduced with permission from ref. 59. Copyright 2021, Elsevier.

NPs with 2-3 atomic thickness Pt skin exhibited enhanced activity.³³ The d-spacing of the Pt {111} skin in this core-shell intermetallic structure is 0.09 Å smaller than that of pure Pt. Such a contraction resulted in an increased overlap of the 5d electron cloud of the surface Pt sites and caused a downward shift of the antibonding states of O-Pt. This weaker binding energy of oxygen intermediates could lead to a high intrinsic ORR activity.

An enhancement in activity was reported for the L1₀-PtCo intermetallic nanowires with high-index facets.²² The L1₀-PtCo nanowire electrocatalyst had a high ratio of {221} facets and exhibited a mass activity of 1.30 A mg_{Pt}^{-1} at 0.9 V (vs. RHE). Theoretical calculations suggested that the {111} terraces of the {221} facets are strained by both the presence of subsurface Co and the nature of high-index facet, resulting in high ORR activity on the fcc hollow (active) sites. The {111} terraces also extended enough to avoid deactivation by interacting with the oxygen species on the step sites.

Multiple structural factors may work synergistically to affect the observed ORR activity. Electrocatalysts made of octahedral L10-PtCo NPs with ultrathin Pt shell had a mass activity of 2.82 A mg_{Pt}^{-1} at 0.9 V (vs. RHE), which is 13 times that of the commercial Pt/C catalyst.97 The authors attributed this large enhancement to three possible reasons. First, the ordered intermetallic structure resulted in strong ligand and stain effects in near-surface regions. 96 Second, the exposure of Pt {111} facets in the octahedral shape exhibited anisotropic strains. Third, the active sites on the surfaces were fully exposed.

Similarly, multiple structural factors help to enhance the durability of the Pt-Co intermetallic electrocatalysts, which include the degree of ordering, 83,122 composition, 111,130,133 particle size, 33,83,94 and core-shell structure. 28,30,93,100 The impact of structural ordering of the Pt-Co catalyst on metal (Pt and Co) dissolution and re-deposition as well as the associated durability under PEMFC operational conditions was revealed by a microscopic study.83 Since the oxidation of surface Pt atoms is often the cause for the dissolution of Pt-based NP electrocatalysts, eliminating the reactive corner and edge sites of L1₀-PtCo NPs by the addition of a less reactive metal such as Au could improve the durability by blocking the oxidation of Pt at these sites. 111,133 The Auincorporated L1₀-PtCo intermetallic electrocatalyst exhibited an initial mass activity of 0.67 A mg_{Pt}^{-1} and ended with a value of 0.64 A mg_{Pt}⁻¹ after 10 k RDE-based AST cycles, showing 97% retention.111

There are various reports on the effects of PtCo particle size on ORR durability. Subsized Pt-Co intermetallic NPs was found to enhance the stability of the membrane electrode by preventing the poisoning by ionomers in humid fuel cells. 33 At the BOL of MEA test, the L1₂-Pt₃Co electrocatalyst exhibited a mass activity of 0.92 A mg_{Pt}^{-1} at 0.9 V (cell voltage), which is six times that of commercial Pt/C. The mass activity reduced to $0.84 \text{ A mg}_{Pt}^{-1}$ (8.7% loss) after 10k cycles and 0.75 A mg $_{Pt}^{-1}$ (18.5% loss) after 30 k cycles in the MEA-based test. The confinement of mesoporous carbon was reported to not only control the particle size of L12-Pt3Co NPs but also mitigate their aggregation during the electrochemical reactions and significantly suppress the detachment of catalyst particles.⁹⁴ The as-made electrocatalysts showed 13.3% loss in mass activity after the RDE-based AST. The MEA made from the same catalyst underwent a 15.4% decrease in current density at 0.6 V (cell voltage) after 20 k cycles, which was less than that of the commercial Pt/C MEA after 10 k cycles (15.8% loss). The L10-PtCo electrocatalyst may retain 77% of its initial mass activity after 30 k AST cycles in MEA if they were anchored strongly on the support through enhanced support-metal interaction. The intermetallic core-shell structure of this catalyst was preserved after the AST, suggesting structural stability.90

In addition, optimized core-shell structure could also contribute to the ORR durability of PtCo intermetallic electrocatalysts.^{28,100} Nine nanometer-sized, hard-magnet L1₀-PtCo NPs with 2-3 atomic layer Pt shell were prepared as the electrocatalysts.³⁰ In RDE tests, the catalysts exhibited a BOL mass activity of 2.26 A mg_{pt}⁻¹, which was 19 times of the commercial Pt/C. The mass activity was 1.88 A mg_{pt}^{-1} after 20 k AST cycles and 1.83 A mg_{pt}^{-1} after 30 k AST cycles. In the MEA tests, the catalysts achieved a mass activity of 0.56 A ${\rm mg_{Pt}}^{-1}$ at the BOL and 0.45 A ${\rm mg_{Pt}}^{-1}$ after 30 k AST cycles. Theoretical calculations attributed the enhanced ORR performance to the biaxial strain induced by the Pt shell. The carbon shell may serve as a protective layer to improve the durability if it is designed in such a way that does not block the active sites of the electrocatalyst. 93 For electrocatalysts consisting of L1₀-PtCo NPs with nitrogen-doped carbon shell, its mass activity retained a high value of 1.36 A mg_{Pt}⁻¹ after 20 k AST cycles in RDE-based tests. This performance value represents a loss of 7% in activity.

The enhanced durability of the Pt-Co intermetallic in MEA was achieved through the control of both size and carbon shell. 91 A small molecule-assisted impregnation approach was used to synthesize various intermetallic NPs. Small molecules

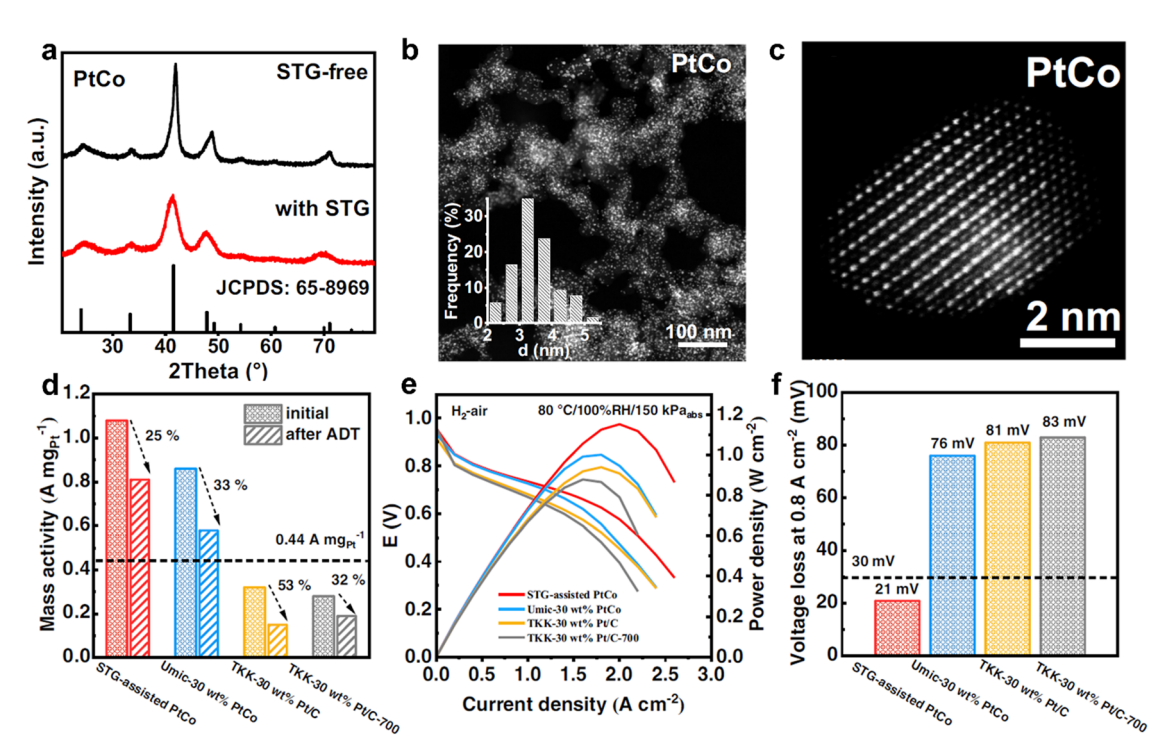


Fig. 11 (a) XRD pattern, (b) HAADF-STEM image (inset: size distribution), and (c) atomic-resolution HAADF-STEM image of PtCo intermetallic NPs. (d) Mass activity loss of different cathode catalysts (STG-assisted PtCo, Umic-30 wt% PtCo, TKK-30 wt% Pt/C, and TKK-30 wt% Pt/C-700) after 30 k cycles. (e) Polarization curves and power density plots in the H_2 -air cell and (f) the voltage loss at 0.8 A cm $^{-2}$. All ORR properties were determined using MEA-based tests. Reproduced with permission from ref. 91. Copyright 2022, Nature Publishing Group.

such as sodium thioglycolate (STG) was added to the metal precursors and sulfur-doped carbon shell coating the intermetallic NPs was formed after annealing. Such a carbon coating successfully suppressed particle sintering and ensured the formation of ultrafine intermetallic NPs (Fig. 11a-c). In H₂-O₂ singlecell test, the STG-assisted L10-PtCo catalyst exhibited a high mass activity of 1.08 A ${\rm mg_{Pt}}^{-1}$ at 0.9 V, which exceeded the US DOE 2025 target of 0.44 A mg_{Pt}^{-1} (Fig. 11d). The mass activity decreased by 25% after 30 k AST cycles in MEA. The STG-assisted L10-PtCo catalyst was tested in a H₂-air single cell at 80 °C, 100% relative humidity (RH), and 150 kPaabs. The current density of the cell was 412 mA cm⁻² at 0.8 V and also exceeded the DOE target of 300 mA cm⁻² (Fig. 11e). After 30 k AST cycles, the voltage loss of STG-assisted L1₀-PtCo catalyst at 0.8 mA cm⁻² was 21 mV, which is below the DOE target of 30 mV loss at the maximum (Fig. 11f). Noticeably, there is a large discrepancy between RDE- and MEAbased results. Further effort is required to enhance the durability of Pt-Co intermetallic electrocatalysts in MEA for practical applications. In addition, it should be noted that besides ORR in this article, Pt-Co intermetallic NPs have also been tested for CO oxidation, 134-138 alcohol oxidation, 56,130 formic acid oxidation, 77 hydrogen evolution reaction,²² and dehydrogenation.⁷⁵

6. Conclusion

In this feature article, we analyze the thermodynamic and kinetic factors governing the preparation of a variety of Pt-Co

based intermetallic NPs. A key aspect to consider is the energy barrier for atomic ordering, which requires heat treatment. Advances in characterization methods enable both in situ and ex situ studies of the atomic ordering process at the nanoscale, thus helping our understanding of the formation mechanism at atomic level. Such studies are often key for uncovering the principles on designing Pt-Co intermetallic with different compositions, size, and shape. The need for producing highly active and durable ORR electrocatalyst drives the development of novel Pt-Co intermetallic with ever-complexing and finely controlled nanostructures. The advantage of using Pt-Co intermetallic electrocatalysts is its durability improvement in PEMFCs.

Although there has been much progress on the Pt-Co intermetallic NP as ORR electrocatalysts in recent years, several challenges remain. Firstly, there is still a major need to develop the methodology for creating highly ordered intermetallic structures as metal segregation and local inhomogeneity often exist in many current products of PtCo intermetallic NPs. In this context, a careful examination of the degree of ordering is required in assessing the crystallinity of the intermetallic structure. The threshold values between the alloy and intermetallic remain unclear. The best practice in analyzing the structure and catalytic performance of Pt-Co intermetallic NPs with different degrees of ordering still needs to be developed. Local inhomogeneity requires accurate and non-destructive characterization methods to analyze the Pt/Co ratio and other key variables. 139 Secondly, for the disorder-to-order transition, there are constraints in the study of atomic ordering mechanism

to only a few scenarios such as thermal annealing because of the limitation of in situ characterization methods. Empirical studies are often the approaches to identify the optimal conditions for atomic ordering. Thirdly, certain Pt-Co intermetallic phase, namely, L12-PtCo3, is theoretically predicted, but there is a lack of experimental reports. 55-57 Thus, the performance of Co-rich intermetallic remains largely unknown. The incorporation of a third metal into the Pt-Co intermetallic NPs raises new possibilities for versatile electrocatalysts. However, similarity between the third metal (i.e., Fe, Ni, Cu, and Ti) and Co atoms makes microscopic characterization difficult; thus, the structural details of these "half-intermetallic" are unclear. Fourthly, the morphologies of current Pt-Co intermetallic are mainly quasi-spherical and partially faceted. The synthesis and property studies of 1D, 2D, and higher-ordered (i.e., hierarchical and porous structures) Pt-Co intermetallic NPs could be intriguing. The synthesis of lowdimensional or complex intermetallic nanostructures are closely related to the understanding of the surface energy control of different facets. Fifthly, for Pt-Co intermetallic electrocatalyst, the MEA durability performance is still far from reaching the maximum or high-activity values demonstrated in the RDE studies. Designing such intermetallic ORR electrocatalysts for MEAs continue to be a challenge. In this context, there is a need to design low-cost testing strategies to understand the degradation mechanisms and effects of electrolytes and operating conditions in a full cell study. While intermetallic Pt-Co nanoparticles are often good electrocatalysts for ORR with high durability, the excess dissolution of Co atoms from L12 Pt3Co intermetallic was observed and attributed to the lack of formation of the Pt skin layer. 140 Thus, additional factors beyond the ordered intermetallic structures should be considered, especially for durability. Development of microscopic characterization methods in dynamic tracking and modeling, reliable prototyping in MEA testing, and bridging techniques to better utilize the RDE test for understanding full cell performances all become increasingly important. 141

Conflicts of interest

There are no conflicts to declare.

Acknowledgements

We would like to thank U.S. National Science Foundation (CBET-2055734, CHE-1213926 and DMR-0449849) for the past and current supports of our studies on synthesis of bimetallic nanoparticles and on electrocatalysis. In addition, we are grateful to our colleagues whose work is presented in this feature article.

Notes and references

- 1 J. Carter, G. McVinker, W. Weissman, M. Kmak and J. Sinfelt, Appl. Catal., 1982, 3, 327-346.
- 2 M. Omrani, M. Goriaux, Y. Liu, S. Martinet, L. Jean-Soro and V. Ruban, Environ. Pollut., 2020, 257, 113477.
- 3 M. Jeyaraj, S. Gurunathan, M. Qasim, M.-H. Kang and J.-H. Kim, Nanomaterials, 2019, 9, 1719.

- 4 J. Wu and H. Yang, Acc. Chem. Res., 2013, 46, 1848-1857.
- 5 Z. Peng and H. Yang, Nano Today, 2009, 4, 143-164.
- 6 J. Peng, P. Tao, C. Song, W. Shang, T. Deng and J. Wu, Chin. I. Catal., 2022, 43, 47-58.
- 7 C. Wang and J. S. Spendelow, Curr. Opin. Electrochem., 2021, 28,
- 8 M. Zhou, C. Li and J. Fang, Chem. Rev., 2021, 121, 736-795.
- 9 J. Greeley, I. Stephens, A. Bondarenko, T. P. Johansson, H. A. Hansen, T. Jaramillo, J. Rossmeisl, I. Chorkendorff and J. K. Nørskov, Nat. Chem., 2009, 1, 552-556.
- 10 X. X. Wang, J. Sokolowski, H. Liu and G. Wu, Chin. J. Catal., 2020, 41, 739-755.
- 11 X. Yu and S. Ye, J. Power Sources, 2007, 172, 145-154.
- 12 P. C. Okonkwo, O. O. Ige, E. M. Barhoumi, P. C. Uzoma, W. Emori, A. Benamor and A. M. Abdullah, Int. J. Hydrog. Energy, 2021, 46, 15850-15865.
- 13 D. A. Cullen, K. C. Neyerlin, R. K. Ahluwalia, R. Mukundan, K. L. More, R. L. Borup, A. Z. Weber, D. J. Myers and A. Kusoglu, Nat. Energy, 2021, 6, 462-474.
- 14 D. Y. Chung, S. W. Jun, G. Yoon, S. G. Kwon, D. Y. Shin, P. Seo, J. M. Yoo, H. Shin, Y.-H. Chung, H. Kim, B. S. Mun, K.-S. Lee, N.-S. Lee, S. J. Yoo, D.-H. Lim, K. Kang, Y.-E. Sung and T. Hyeon, J. Am. Chem. Soc., 2015, 137, 15478-15485.
- 15 T. Y. Yoo, J. M. Yoo, A. K. Sinha, M. S. Bootharaju, E. Jung, H. S. Lee, B.-H. Lee, J. Kim, W. H. Antink, Y. M. Kim, J. Lee, E. Lee, D. W. Lee, S.-P. Cho, S. J. Yoo, Y.-E. Sung and T. Hyeon, J. Am. Chem. Soc., 2020, 142, 14190-14200.
- 16 Z. Zhao, Z. Liu, A. Zhang, X. Yan, W. Xue, B. Peng, H. L. Xin, X. Pan, X. Duan and Y. Huang, Nat. Nanotechnol., 2022, 17, 968-975.
- 17 Y. Zhu, J. Peng, X. Zhu, L. Bu, Q. Shao, C.-W. Pao, Z. Hu, Y. Li, J. Wu and X. Huang, Nano Lett., 2021, 21, 6625-6632.
- 18 J. Wu, J. Zhang, Z. Peng, S. Yang, F. T. Wagner and H. Yang, J. Am. Chem. Soc., 2010, 132, 4984-4985.
- 19 C. Chen, Y. Kang, Z. Huo, Z. Zhu, W. Huang, H. L. Xin, J. D. Snyder, D. Li, J. A. Herron, M. Mavrikakis, M. Chi, K. L. More, Y. Li, N. M. Markovic, G. A. Somorjai, P. Yang and V. R. Stamenkovic, Science, 2014, 343, 1339-1343.
- 20 H. Y. Kim, M. Jun, S. H. Joo and K. Lee, ACS Nanosci. Au, 2023, 3, 28-36.
- 21 T.-H. Yang, J. Ahn, S. Shi, P. Wang, R. Gao and D. Qin, Chem. Rev., 2021, 121, 796-833.
- 22 E. B. Tetteh, C. Gyan-Barimah, H.-Y. Lee, T.-H. Kang, S. Kang, S. Ringe and J.-S. Yu, ACS Appl. Mater. Interfaces, 2022, 14, 25246-25256.
- 23 Y.-T. Pan and H. Yang, Nano Today, 2020, 31, 100832.
- 24 Z. Xia and S. Guo, Chem. Soc. Rev., 2019, 48, 3265-3278.
- 25 P. Strasser, S. Koh, T. Anniyev, J. Greeley, K. More, C. Yu, Z. Liu, S. Kaya, D. Nordlund, H. Ogasawara, M. F. Toney and A. Nilsson, Nat. Chem., 2010, 2, 454-460.
- 26 V. Stamenkovic, B. S. Mun, K. J. Mayrhofer, P. N. Ross, N. M. Markovic, J. Rossmeisl, J. Greeley and J. K. Nørskov, Angew. Chem., 2006, 118, 2963-2967.
- 27 V. R. Stamenkovic, B. S. Mun, M. Arenz, K. J. Mayrhofer, C. A. Lucas, G. Wang, P. N. Ross and N. M. Markovic, Nat. Mater., 2007, 6, 241-247.
- 28 D. Wang, H. L. Xin, R. Hovden, H. Wang, Y. Yu, D. A. Muller, F. J. DiSalvo and H. D. Abruña, Nat. Mater., 2013, 12, 81-87.
- 29 S. Dai, Y. You, S. Zhang, W. Cai, M. Xu, L. Xie, R. Wu, G. W. Graham and X. Pan, Nat. Commun., 2017, 8, 1-8.
- 30 J. Li, S. Sharma, X. Liu, Y.-T. Pan, J. S. Spendelow, M. Chi, Y. Jia, P. Zhang, D. A. Cullen, Z. Xi, H. Lin, Z. Yin, B. Shen, M. Muzzio, C. Yu, Y. S. Kim, A. A. Peterson, K. L. More, H. Zhu and S. Sun, Joule, 2019, 3, 124-135.
- 31 H. L. Xin, S. Alayoglu, R. Tao, A. Genc, C.-M. Wang, L. Kovarik, E. A. Stach, L.-W. Wang, M. Salmeron, G. A. Somorjai and H. Zheng, Nano Lett., 2014, 14, 3203-3207.
- 32 M. Chi, C. Wang, Y. Lei, G. Wang, D. Li, K. L. More, A. Lupini, L. F. Allard, N. M. Markovic and V. R. Stamenkovic, Nat. Commun., 2015, 6, 1-9.
- 33 H. Cheng, R. Gui, H. Yu, C. Wang, S. Liu, H. Liu, T. Zhou, N. Zhang, X. Zheng, W. Chu, Y. Lin, H. Wu, C. Wu and Y. Xie, Proc. Natl. Acad. Sci. U. S. A., 2021, 118, e2104026118.
- 34 S. Lee, J.-H. Jang, I. Jang, D. Choi, K.-S. Lee, D. Ahn, Y. S. Kang, H.-Y. Park and S. J. Yoo, J. Catal., 2019, 379, 112-120.

ChemComm Feature Article

- 35 G. Tritsaris, J. Greeley, J. Rossmeisl and J. K. Nørskov, *Catal. Lett.*, 2011, **141**, 909–913.
- 36 D. J. S. Sandbeck, N. M. Secher, F. D. Speck, J. E. Sørensen, J. Kibsgaard, I. Chorkendorff and S. Cherevko, ACS Catal., 2020, 10, 6281–6290.
- 37 The fuel cell technologies office multi-year research, development, and demonstration plan, https://www.energy.gov/sites/prod/files/ 2014/12/f19/fcto_myrdd_full_document.pdf).
- 38 S. Stariha, N. Macauley, B. T. Sneed, D. Langlois, K. L. More, R. Mukundan and R. L. Borup, J. Electrochem. Soc., 2018, 165, F492–F501.
- 39 L. Chong, J. Wen, J. Kubal, F. G. Sen, J. Zou, J. Greeley, M. Chan, H. Barkholtz, W. Ding and D.-J. Liu, *Science*, 2018, 362, 1276–1281.
- 40 T. Yoshida and K. Kojima, Electrochem. Soc. Interface, 2015, 24, 45-49.
- 41 E. Antolini, Appl. Catal., B, 2017, 217, 201-213.
- 42 S. Furukawa and T. Komatsu, ACS Catal., 2017, 7, 735-765.
- 43 M. Luo, Y. Sun, L. Wang and S. Guo, Adv. Energy Mater., 2017, 7, 1602073.
- 44 Y. Yan, J. S. Du, K. D. Gilroy, D. Yang, Y. Xia and H. Zhang, Adv. Mater., 2017, 29, 1605997.
- 45 J. Li and S. Sun, Acc. Chem. Res., 2019, 52, 2015-2025.
- 46 L. Rößner and M. Armbrüster, ACS Catal., 2019, 9, 2018-2062.
- 47 H. Y. Kim and S. H. Joo, J. Mater. Chem. A, 2020, 8, 8195-8217.
- 48 J. Zhang, L. Shen, Y. Jiang and S. Sun, *Nanoscale*, 2020, 12, 19557–19581.
- 49 X. Li, J. Zhao and D. Su, Small Struct., 2021, 2, 2100011.
- 50 Y. Yuan, Z. Yang, W. Lai, L. Gao, M. Li, J. Zhang and H. Huang, *Chem. Eur. J.*, 2021, 27, 16564–16580.
- 51 J. Bai, L. Yang, Z. Jin, J. Ge and W. Xing, Chin. J. Catal., 2022, 43, 1444–1458.
- 52 X. Liu, J. Liang and Q. Li, Chin. J. Catal., 2023, 45, 17–26.
- 53 H. Chen, J. Liu, X. Wu, C. Ye, J. Zhang, J. L. Luo and X. Z. Fu, Small, 2022, 18, 2204100.
- 54 D. Kim, J. E. Saal, L. Zhou, S. Shang, Y. Du and Z.-K. Liu, *CALPHAD: Comput. Coupling Phase Diagrams Thermochem.*, 2011, 35, 323–330.
- 55 S. Wang, W. Xu, Y. Zhu, Q. Luo, C. Zhang, S. Tang and Y. Du, ACS Appl. Mater. Interfaces, 2021, 13, 827–835.
- 56 B. Shen, L. Huang, J. Shen, K. He, C. Y. Zheng, V. P. Dravid, C. Wolverton and C. A. Mirkin, *Proc. Natl. Acad. Sci. U. S. A.*, 2021, 118, e2105722118.
- 57 Z. Wang, X. Yao, Y. Kang, L. Miao, D. Xia and L. Gan, Adv. Funct. Mater., 2019, 29, 1902987.
- 58 K. H. J. Buschow, P. G. van Engen and R. Jongebreur, J. Magn. Magn. Mater., 1983, 38, 1–22.
- 59 Y. Ma, A. N. Kuhn, W. Gao, T. Al-Zoubi, H. Du, X. Pan and H. Yang, Nano Energy, 2021, 79, 105465.
- 60 J. D. Lee, D. Jishkariani, Y. Zhao, S. Najmr, D. Rosen, J. M. Kikkawa, E. A. Stach and C. B. Murray, ACS Appl. Mater. Interfaces, 2019, 11, 26789–26797.
- 61 Y. Xiong, Y. Yang, H. Joress, E. Padgett, U. Gupta, V. Yarlagadda, D. N. Agyeman-Budu, X. Huang, T. E. Moylan, R. Zeng, A. Kongkanand, F. A. Escobedo, J. D. Brock, F. J. DiSalvo, D. A. Muller and H. D. Abruña, *Proc. Natl. Acad. Sci. U. S. A.*, 2019, 116, 1974–1983.
- 62 Y. Liao, Y. Wang, J. Liu, Y. Tang, C. Wu and Y. Chen, *Ind. Eng. Chem. Res.*, 2021, 60, 14728–14736.
- 63 F. Li, Y. Zong, Y. Ma, M. Wang, W. Shang, P. Tao, C. Song, T. Deng, H. Zhu and J. Wu, ACS Nano, 2021, 15, 5284–5293.
- 64 X. Li, Y. He, S. Cheng, B. Li, Y. Zeng, Z. Xie, Q. Meng, L. Ma, K. Kisslinger, X. Tong, S. Hwang, S. Yao, C. Li, Z. Qiao, C. Shan, Y. Zhu, J. Xie, G. Wang, G. Wu and D. Su, *Adv. Mater.*, 2021, 33, 2106371.
- 65 X. Li, S. Cheng, Y. He, L. Qian, D. Zakharov, G. Wu, C. Shan, L. Zhang and D. Su, *Nano Res.*, 2023, 16, 3055–3062.
- 66 Y.-T. Pan, Y. Yan, Y.-T. Shao, J.-M. Zuo and H. Yang, *Nano Lett.*, 2016, 16, 6599–6603.
- 67 J. Wu, W. Gao, J. Wen, D. J. Miller, P. Lu, J.-M. Zuo and H. Yang, Nano Lett., 2015, 15, 2711–2715.
- 68 J. Wu, H. Shan, W. Chen, X. Gu, P. Tao, C. Song, W. Shang and T. Deng, *Adv. Mater.*, 2016, 28, 9686–9712.
- 69 K. Wang, L. Wang, Z. Yao, L. Zhang, L. Zhang, X. Yang, Y. Li, Y.-G. Wang, Y. Li and F. Yang, Sci. Adv., 2022, 8, eabo4599.
- 70 K. Aso, H. Kobayashi, S. Yoshimaru, X. Q. Tran, M. Yamauchi, S. Matsumura and Y. Oshima, *Nanoscale*, 2022, 14, 9842–9848.

- 71 T. Kaito, H. Tanaka, H. Mitsumoto, S. Sugawara, K. Shinohara, H. Ariga, H. Uehara, S. Takakusagi and K. Asakura, J. Phys. Chem. C, 2016, 120, 11519–11527.
- 72 W.-J. Zeng, C. Wang, Q.-Q. Yan, P. Yin, L. Tong and H.-W. Liang, Nat. Commun., 2022, 13, 7654.
- 73 H. Liao, A. Fisher and Z. Xu, Small, 2015, 11, 3221–3246.
- 74 S. Prabhudev, M. Bugnet, C. Bock and G. A. Botton, ACS Nano, 2013, 7, 6103–6110.
- 75 L. G. Cesar, C. Yang, Z. Lu, Y. Ren, G. Zhang and J. T. Miller, ACS Catal., 2019, 9, 5231–5244.
- 76 Y. Hu, X. Guo, T. Shen, Y. Zhu and D. Wang, ACS Catal., 2022, 12, 5380–5387.
- 77 L. Chen, J. Zhu, C. Xuan, W. Xiao, K. Xia, W. Xia, C. Lai, H. L. Xin and D. Wang, *J. Mater. Chem. A*, 2018, **6**, 5848–5855.
- 78 W. Zhao, B. Chi, L. Liang, P. Yang, W. Zhang, X. Ge, L. Wang, Z. Cui and S. Liao, ACS Catal., 2022, 12, 7571–7578.
- 79 C. Li, W. Zhao, X. Lu, Z. Chen, B. Han, X. Zhang, J. Chen, Y. Shao, J. Huo, Y. Zhu, Y. Deng, S. Sun and S. Liao, *J. Energy Chem.*, 2023, 78, 340–349.
- 80 J. Liang, N. Li, Z. Zhao, L. Ma, X. Wang, S. Li, X. Liu, T. Wang, Y. Du, G. Lu, J. Han, Y. Huang, D. Su and Q. Li, *Angew. Chem., Int. Ed.*, 2019, 58, 15471–15477.
- 81 L. Zhang, X. Ji, X. Wang, Y. Fu, H. Zhu and T. X. Liu, *J. Electrochem. Soc.*, 2020, **167**, 024507.
- 82 Y. Jin, G. Ren, Y. Feng, S. Geng, L. Li, X. Zhu, J. Guo, Q. Shao, Y. Xu, X. Huang and J. Lu, *Nano Res.*, 2022, **15**, 9631–9638.
- 83 Y. Cui, Y. Wu, Z. Wang, X. Yao, Y. Wei, Y. Kang, H. Du, J. Li and L. Gan, J. Electrochem. Soc., 2020, 167, 064520.
- 84 W.-J. Zeng, L. Tong, J. Liu and H.-W. Liang, J. Electroanal. Chem., 2022, 922, 116728.
- 85 T.-W. Song, L.-J. Zuo, M. Zuo and H.-W. Liang, J. Catal., 2023, 419, 19–25.
- 86 W. Xu, Z. Zhu, Y. Wang, P. Cui, L. Tong, K. Zhao, J. Yuan, Z.-Y. Zhou, H.-W. Liang, N. Tian and S.-G. Sun, J. Mater. Chem. A, 2023, 11, 4078–4087.
- 87 S. Hu and W.-X. Li, Science, 2021, 374, 1360-1365.
- 88 M. Wang, M. Wang, L. Guo, Y. Li, S. Chen and Z. Wei, *Int. J. Hydrogen Energy*, 2022, 47, 27116–27123.
- 89 S.-L. Xu, S.-C. Shen, S. Zhao, Y.-W. Ding, S.-Q. Chu, P. Chen, Y. Lin and H.-W. Liang, *Chem. Sci.*, 2020, **11**, 7933–7939.
- 90 C.-L. Yang, L.-N. Wang, P. Yin, J. Liu, M.-X. Chen, Q.-Q. Yan, Z.-S. Wang, S.-L. Xu, S.-Q. Chu, C. Cui, H. Ju, J. Z. Zhu, Y. L. Lin, J. Shui and H.-W. Liang, *Science*, 2021, 374, 459–464.
- 91 T.-W. Song, C. Xu, Z.-T. Sheng, H.-K. Yan, L. Tong, J. Liu, W.-J. Zeng, L.-J. Zuo, P. Yin, M. Zuo, S.-Q. Chu, P. Chen and H.-W. Liang, *Nat. Commun.*, 2022, 13, 1–11.
- 92 Y. Zhao, C. Wang, J. Liu and F. Wang, Nanoscale, 2018, 10, 9038-9043.
- 93 M. Chen, S. Zhou, W. Liao, Z. Wang, J. Long, Q. Zhou and Q. Wang, ChemElectroChem, 2022, 9, e202200803.
- 94 W. Zhao, Y. Ye, W. Jiang, J. Li, H. Tang, J. Hu, L. Du, Z. Cui and S. Liao, J. Mater. Chem. A, 2020, 8, 15822–15828.
- 95 H. Zhong, H. Wu, Y. Pan, H. Li, Y. Peng, D. Banham and J. Zeng, Int. J. Hydrogen Energy, 2022, 47, 40952–40960.
- 96 Y. Liao, L. Peng, C. Wu, Y. Yan, H. Xie, Y. Chen and Y. Wang, *Nano Res.*, 2023, DOI: 10.1007/s12274-023-5399-2.
- 97 M. Xie, Z. Lyu, R. Chen, M. Shen, Z. Cao and Y. Xia, J. Am. Chem. Soc., 2021, 143, 8509–8518.
- 98 R. Toyama, S. Kawachi, J.-I. Yamaura, T. Fujita, Y. Murakami, H. Hosono and Y. Majima, *Nanoscale Adv.*, 2022, 4, 5270–5280.
- 99 H. Y. Kim, J. M. Kim, Y. Ha, J. Woo, A. Byun, T. J. Shin, K. H. Park, H. Y. Jeong, H. Kim, J. Y. Kim and S. H. Joo, ACS Catal., 2019, 9, 11242–11254.
- 100 Y. Cai, P. Gao, F. Wang and H. Zhu, Electrochim. Acta, 2017, 245, 924-933.
- 101 W. Yang, L. Zou, Q. Huang, Z. Zou, Y. Hu and H. Yang, J. Electrochem. Soc., 2017, 164, H331–H337.
- 102 Y. Xiong, L. Xiao, Y. Yang, F. J. DiSalvo and H. D. Abruña, *Chem. Mater.*, 2018, 30, 1532–1539.
- 103 T. He, W. Wang, X. Yang, F. Shi, Z. Ye, Y. Zheng, F. Li, J. Wu, Y. Yin and M. Jin, *ACS Nano*, 2021, **15**, 7348–7356.
- 104 Q. Cheng, S. Yang, C. Fu, L. Zou, Z. Zou, Z. Jiang, J. Zhang and H. Yang, *Energy Environ. Sci.*, 2022, 15, 278–286.
- 105 Y.-H. Wen, L.-H. Zhang, J.-B. Wang and R. Huang, J. Alloys Compd., 2019, 776, 629–635.

- 106 W. Liu, S. Di, F. Wang and H. Zhu, Int. J. Hydrogen Energy, 2022, 47, 6312-6322.
- D. J. Rosen, A. C. Foucher, J. D. Lee, S. Yang, E. Marino, E. A. Stach and C. B. Murray, ACS Mater. Lett., 2022, 4, 823-830.
- 108 H. You, S. Yang, B. Ding and H. Yang, Chem. Soc. Rev., 2013, 42,
- 109 Y. Xiong, Y. Yang, F. J. DiSalvo and H. D. Abruña, ACS Nano, 2020, 14, 13069-13080.
- 110 X. X. Wang, S. Hwang, Y.-T. Pan, K. Chen, Y. He, S. Karakalos, H. Zhang, J. S. Spendelow, D. Su and G. Wu, Nano Lett., 2018, 18, 4163-4171.
- 111 K. A. Kuttiyiel, S. Kattel, S. Cheng, J. H. Lee, L. Wu, Y. Zhu, G.-G. Park, P. Liu, K. Sasaki, J. G. Chen and R. R. Adzic, ACS Appl. Energy Mater., 2018, 1, 3771-3777.
- 112 X.-F. Han, N. Batool, W.-T. Wang, H.-T. Teng, L. Zhang, R. Yang and J.-H. Tian, ACS Appl. Mater. Interfaces, 2021, 13, 37133-37141.
- 113 M. Liu, A. Hu, Y. Ma, G. Wang, L. Zou, X. Chen and H. Yang, J. Electroanal. Chem., 2020, 871, 114267.
- 114 W. H. Lai, B. W. Zhang, Z. Hu, X. M. Qu, Y. X. Jiang, Y. X. Wang, J. Z. Wang, H. K. Liu and S. L. Chou, Adv. Funct. Mater., 2019, 29, 1807340.
- 115 L. Pavko, M. Gatalo, G. Križan, J. Križan, K. Ehelebe, F. Ruiz-Zepeda, M. Sala, G. Dražić, M. Geuß, P. Kaiser, M. Bele, M. Kostelec, T. Đukić, N. Van de Velde, I. Jerman, S. Cherevko, N. Hodnik, B. Genorio and M. Gaberšček, ACS Appl. Energy Mater., 2021, 4, 13819–13829.
- 116 M. Vondrova, C. M. Burgess and A. B. Bocarsly, Chem. Mater., 2007, 19, 2203-2212.
- 117 J. Li, S. Sharma, K. Wei, Z. Chen, D. Morris, H. Lin, C. Zeng, M. Chi, Z. Yin, M. Muzzio, M. Shen, P. Zhang, A. A. Peterson and S. Sun, J. Am. Chem. Soc., 2020, 142, 19209-19216.
- 118 V. R. Stamenkovic, B. Fowler, B. S. Mun, G. Wang, P. N. Ross, C. A. Lucas and N. M. Markovic, Science, 2007, 315, 493-497.
- 119 X. Huang, Z. Zhao, L. Cao, Y. Chen, E. Zhu, Z. Lin, M. Li, A. Yan, A. Zettl, Y. M. Wang, X. Duan, T. Mueller and Y. Huang, Science, 2015, 348, 1230-1234.
- 120 R. Huang, G.-F. Shao, Y. Zhang and Y.-H. Wen, ACS Appl. Mater. Interfaces, 2017, 9, 12486-12493.
- 121 Y.-H. Wen and R. Huang, J. Phys. Chem. C, 2019, 123, 12007–12014.
- 122 Y.-T. Pan, D. Li, S. Sharma, C. Wang, M. J. Zachman, E. C. Wegener, A. J. Kropf, Y. S. Kim, D. J. Myers, A. A. Peterson, D. A. Cullen and J. S. Spendelow, Chem. Catal., 2022, 2, 3559-3572.

- 123 W. S. Jung, W. H. Lee, H.-S. Oh and B. N. Popov, J. Mater. Chem. A, 2020, 8, 19833-19842.
- 124 L. Chen, J. Zhu, J. Wang, W. Xiao, W. Lei, T. Zhao, T. Huang, Y. Zhu and D. Wang, Electrochim. Acta, 2018, 283, 1253-1260.
- 125 Z. Qiao, C. Wang, C. Li, Y. Zeng, S. Hwang, B. Li, S. Karakalos, J. Park, A. J. Kropf, E. C. Wegener, Q. Gong, H. Xu, G. Wang, D. J. Myers, J. Xie, J. S. Spendelow and G. Wu, Energy Environ. Sci., 2021, 14, 4948-4960.
- 126 L.-C. Lin, C.-H. Kuo, Y.-H. Hsu, L.-C. Hsu, H.-Y. Chen, J.-L. Chen and Y.-T. Pan, Appl. Catal., B, 2022, 317, 121767.
- 127 P. Ren, P. Pei, Y. Li, Z. Wu, D. Chen and S. Huang, Prog. Energy Combust. Sci., 2020, 80, 100859.
- 128 Q. Gong, H. Zhang, H. Yu, S. Jeon, Y. Ren, Z. Yang, C.-J. Sun, E. A. Stach, A. C. Foucher, Y. Yu, M. Smart, G. M. Filippelli, D. A. Cullen, P. Liu and J. Xie, Matter, 2023, 6, 963-982.
- 129 Y. Zhao, J. Liu, Y. Zhao, F. Wang and Y. Song, J. Mater. Chem. A, 2015, 3, 20086-20091.
- 130 J. Gao, X. Zhou, Y. Wang, Y. Chen, Z. Xu, Y. Qiu, Q. Yuan, X. Lin and H. J. Qiu, Small, 2022, 18, 2202071.
- 131 P. Guo, Y. Xia, B. Liu, M. Ma, L. Shen, Y. Dai, Z. Zhang, Z. Zhao, Y. Zhang, L. Zhao and Z. Wang, ACS Appl. Mater. Interfaces, 2022, 14, 53819-53827.
- 132 T. Ellaby, A. Varambhia, X. Luo, L. Briquet, M. Sarwar, D. Ozkaya, D. Thompsett, P. D. Nellist and C.-K. Skylaris, Phys. Chem. Chem. Phys., 2020, 22, 24784-24795.
- 133 L. Zhang, X. Wang and H. Zhu, Prog. Nat. Sci.: Mater. Int., 2020, 30, 890-895.
- 134 X. Song, L. Huang, W. He, C. Liu, F. Hu, Y. Jiang, Z. Sun and S. Wei, J. Phys. Chem. C, 2019, 123, 10907-10916.
- 135 T. Komatsu and A. Tamura, J. Catal., 2008, 258, 306-314.
- 136 H. Li, X. Yu, S.-T. Tu, J. Yan and Z. Wang, Appl. Catal., A, 2010, 387,
- 137 X. Yu, H. Li, S.-T. Tu, J. Yan and Z. Wang, Int. J. Hydrogen Energy, 2011, 36, 3778-3788.
- 138 S. Furukawa, K. Ehara and T. Komatsu, Catal. Sci. Technol., 2016, 6, 1642-1650.
- 139 S. A. Davari, S. Hu and D. Mukherjee, Talanta, 2017, 164, 330-340.
- 140 H. Yano, I. Arima, M. Watanabe, A. Iiyama and H. Uchida, J. Electrochem. Soc., 2017, 164, F966-F972.
- 141 Y. Yu, H. L. Xin, R. Hovden, D. Wang, E. D. Rus, J. A. Mundy, D. A. Muller and H. D. Abruña, Nano Lett., 2012, 12, 4417-4423.